Università degli Studi di Trieste

Dipartimento di Fisica

Scuola di Dottorato in Fisica

Carbon dioxide adsorption and hydrogenation on nickel-based surfaces: a first principles study

Dottorando:

Michele Rizzi

Tutor:

Prof. M.Peressi

Marzo 2011

Abstract

The chemistry of carbon dioxide has recently become of great interest both for technological and environmental issues. Indeed, carbon dioxide is one of the most problematic greenhouse gases and is also a fundamental ingredient for the industrial catalytic organic synthesis of many compounds like, for example, methanol. Recent investigations have shown that, while the common industrial process for methanol synthesis is carried out on Cu catalysts, Ni-Cu model catalysts show a particularly high efficiency. In order to understand the origin of such increase in the catalyst activity, a thorough characterization of the CO_2 -Ni interaction and the atomic-scale description of the hydrogenation process are mandatory. This thesis is focused on the study of the adsorption and activation of carbon dioxide mainly on pure Ni(110) surface and of its reactions with atomic and molecular hydrogen by means of accurate quantum mechanical first principles numerical simulations. The interaction of the CO_2 molecule with the surface is characterized in terms of adsorption geometries, energetics, vibrational and electronic properties, including charge transfer, core-level shifts and scanning tunneling microscopy images, obtained from electronic structure calculations and compared with original experimental results achieved mainly by the Surface Structure and Reactivity Group active at the TASC laboratory. A consistent picture of CO_2 chemisorption on Ni(110) is provided on the basis of the newly available information, yielding a deeper insight into the previously existing spectroscopic and theoretical data. We find that CO_2 molecule can be chemisorbed in different, almost energetically equivalent adsorption configurations on a Ni(110) surface,

with high charge transfer from the substrate. The molecule, that in gas phase is linear and unreactive, is chemisorbed in a bent and activated state on the nickel surface and can react with the hydrogen. The atomic-scale investigation sheds light also on the long-standing debate on the actual reaction path followed by the reactants. Different hydrogenation channels have been explored to determine the reaction network: using molecular hydrogen, only a Langmuir-Hinshelwood process (both reactants are adsorbed) is possible, resulting in the production of formate which is just a 'dead-end' molecule; with atomic hydrogen, instead, the reaction proceeds also through parallel Eley-Rideal channels (only one of the molecules adsorbs and the other one reacts with it directly from the gas phase, without adsorbing), where hydrogen-assisted C-O bond cleavage in CO_2 yields CO already at low temperature.

Contents

1 Introduction **2**

2 Theoretical methods **6**

2.1 Ab initio electronic structure calculations 6

2.1.1 The Born-Oppenheimer approximation 7

2.1.2 Density-Functional Theory 9

2.2 Thermally activated processes and Nudged Elastic Band 13

2.2.1 Computational details 16

3 Gas phase CO_2 molecule and Ni(110) surface **18**

3.1 Gas phase carbon dioxide molecule 18

3.2 Ni(110) surface 22

4 CO_2 adsorption on Ni(110) **25**

4.1 Technicalities 25

4.2 Energetics and geometry 27

4.3 Electronic structure 36

4.3.1 Charge 36

4.3.2 Density of states 38

4.4 STM imaging 42

4.4.1 Experimental LT-STM 42
4.4.2 DFT simulations 43
4.5 Vibrational properties and zero point energy 47
4.6 Energy barriers 50

5 Hydrogen assisted transformations of CO_2 on Ni(110) 54
5.1 Simulations 55
5.1.1 Technicalities 55
5.1.2 Langmuir-Hinshelwood reactions 56
5.1.3 Eley-Rideal reactions 59
5.2 Experimental results 60

6 Conclusion 65

Bibliography 69

Acknowledgments 78

Acronyms

DFT Density Functional Theory

DFT-D Density Functional Theory for Dispersion forces

DOS Density of States

GGA Generalized Gradient Approximation

HREELS High Resolution Electron Energy Loss Spectroscopy

UHV Ultra Hight Vacuum

LDA Local Density Approximation

LT-STM Low Temperature Scanning Tunneling Microscopy

MEP Minimum Energy Path

NEB Nudged Elastic Band

PDOS Projected Density of States

STM Scanning Tunneling Microscopy

TPD Temperature Programmed Desorption

TST Transition State Theory

XPS X-ray photoelectron spectroscopy

ZPE Zero Point Energy

Chapter 1

Introduction

The adsorption of CO_2 on different metal surfaces has been the subject of several theoretical and experimental investigations. It is known that, in addition to a physisorbed state, CO_2 is also chemisorbed on Ni(110) under ultra high UHV conditions, while this is not the case for other metal surfaces, where alkali metal co-adsorption is necessary to promote the formation of a chemical bond [1, 2] The case of CO_2/Ni(110) has been revisited in [3, 4] where chemisorption sites and geometries have been identified with respect to those previously known [2, 5, 1, 6]. However, before the work of this thesis, many aspects of CO_2 interaction with the metal were not still fully understood and required further investigations. Concerning the knowledge of the interaction of CO_2 with Ni(110) surface , we can state that:

- Direct experimental observation of the geometry of the chemisorbed molecule was lacking, since the CO_2 overlayer did not show any ordering, thus precluding the use of conventional structural methods based on diffraction.

- The nature of the CO_2 bond with Ni was unknown, a part from a large electron charge transfer occurring from the metal to the molecule, accompanied by

molecule bending and weak binding.

The first aim of this thesis, is to further shed light on the chemisorption geometries and energies of CO_2 on Ni(110), comparing not only vibrational properties and adsorption energies with experimental HREELS and TPD spectra, but also simulated images with experimental low-T STM images. The purpose is to obtain a detailed characterization of the adsorption geometries by direct observation and the best estimate of the energies corresponding to the different adsorbed states.

The second aspect of chemisorbed CO_2 concerns its chemical reactivity. Hydrogenation of carbon dioxide is a key reaction for methanol and, generally, organic synthesis. Methanol is industrially obtained mainly using Cu-based catalysts in a $CO + H_2 + CO_2$ stream. Isotope studies indicated that CO_2 is the carbon and oxygen source [7, 8]. However, very little is known about the microscopic mechanisms of the CO_2 hydrogenation. Recently, a theoretical study about the CO, H_2 and CO_2 chemistry at the Cu(111) surface has appeared [9] indicating a high (about 1 eV) hydrogenation barrier for CO_2 on Cu(111). At high pressure the $H_2 + CO_2$ reaction on Ni can be used for CO_2 conversion into hydrocarbons, methane being the major product [10]. A Ni-Cu alloy has been shown to be a more active catalyst for methanol synthesis at Ni sites than at Cu ones [11, 12, 13]: this is why, in this thesis, we focus on the H- CO_2 -Ni interaction.

Under standard conditions in industrial catalysis [14] as well as upon hydrogen and CO_2 co-adsorption on Ni(110) under UHV conditions, formate has been identified as a stable intermediate [1]. A recent work [15] combining experimental and theoretical investigations based on energetics and vibrational properties con-

firmed this finding, giving further details about the atomic-scale mechanism of CO_2 activation and first hydrogenation on Ni(110). At low T, CO_2 is negatively charged and is chemically bonded mainly via the carbon atom. The molecule receives electronic charge from the metal, bends, and binds to the surface in a 'V' configuration with the carbon atom. When adsorbed H approaches CO_2 , the H- CO_2 complex flips and binds to the surface with the two oxygen atoms and H binds to the carbon atom, thus yielding the formate. The resulting energy barrier for its hydrogenation is relatively small, 0.43 eV. The presence of hydrogen steers the reaction in the desired direction and prevents the formation of CO which, in analogy to what reported for the catalytic system at high pressure, is unreactive. This is the key point of CO_2 + H chemistry on Ni(110), since the charge transfer from the metal to the molecule yields an activated state which is reactive with hydrogen via an induced flip of the complex. This process is quite different with respect to the case of Cu(111) [9], where hydrogen reacts with the CO_2 molecule which remains linear and not activated due to the very weak metal-CO_2 interaction. These investigations have considerably improved the understanding of mechanisms of the first hydrogenation reaction and have clearly indicated the formation of formate but the subsequent hydrogenation steps of CO_2 and the stability of possible intermediates have not yet been analyzed. The aim of this thesis concerning the reactivity of chemisorbed CO_2 on Ni(110) is therefore to improve our knowledge concerning the complete reaction path during catalytic hydrogenation on Ni(110) and investigate whether formate is a stable intermediate or just a spectator to the reaction path.

The standard approach to this system, by means of UHV-based surface science techniques and a beam of molecular hydrogen, is therefore affected by the well

recognized 'pressure gap' problem. Indeed, atomic hydrogen has not yet been used as a reactant under UHV conditions to study this reaction. The atomic gas phase hydrogen has kinetic energy larger than the adsorbed one (at least 2.6 eV, that is the adsorption energy of H on Ni(110)) so considering atomic hydrogen we can mimic higher pressure condition and explore new reaction paths. For this reason in this thesis we also studied the reaction taking place between adsorbed CO_2 and atomic hydrogen approaching the molecule from the vacuum and not from the surface.

This thesis is organized as follows: in the first chapter we briefly discuss about theoretical methods used in simulations. The second and the third chapters contain benchmark calculations about geometrical end electronic properties of the gas phase CO_2 molecule (neutral and charged) and clean Ni(110) surface. In the fourth chapter we discuss the adsorption of CO_2 on Ni(110) surface. We start with the results about adsorption geometries and energies. After the analysis of the electronic structure of the CO_2 /Ni(110) system,we report the result of a study of STM images comparing several simulated images with the experimental ones. In this chapter we will also discuss vibrational properties, activation and diffusion energy barriers of the adsorbed CO_2 , comparing our results with those of TPD, XPS and HREELS experiments. The fifth chapter is devoted to the study of the hydrogenation of the chemisorbed CO_2 activated species. We present the results of our simulations for two kinds of reactions: those that occur between coadsorbed H and CO_2 and those that take place between gas phase hydrogen and adsorbed CO_2 . We construct a reasonable reaction network comparing the results of our simulations with the experimental results. The last chapter contains the conclusions.

Chapter 2

Theoretical methods

In this chapter theoretical concepts which are the basis of ab-initio methods, used to study catalytic processes, are introduced. In particular, all quantities which allow to identify and characterize catalysts, reactants, products and the reaction pathways have been calculated in this work on the basis of Density Functional Theory, as implemented in the Quantum Espresso package [16]. Therefore, in this chapter the basic ideas of Born-Oppenheimer approximation and DFT are presented, together with the use of plane waves to represent electron wavefunctions and density, and ultrasoft pseudopotentials techniques needed to deal with core electrons. Finally, a description of thermally activated processes and Nudged Elastic Band (NEB) method, used to calculate reaction barriers, is presented.

2.1 Ab initio electronic structure calculations

Our electronic structure calculation are based on the Born-Oppenheimer approximation for the separation of the electronic and ionic degrees of freedom and the density-functional theory for the solution of the electronic problem. The approach

chosen has the advantage that interatomic interactions are evaluated in a fully ab initio framework with no adjustable parameters, i.e., no empirical atom-atom potential is used.

2.1.1 The Born-Oppenheimer approximation

The study of a physical system made of M ions and N electrons requires the solution of the Schrödinger equation:

$$H\Psi = W\Psi \tag{2.1}$$

with:

$$H = -\sum_{i=1}^{N} \frac{\hbar^2}{2m_e}\nabla^2_{\mathbf{r}_i} - \sum_{j=1}^{M} \frac{\hbar^2}{2M_j}\nabla^2_{\mathbf{R}_j} - \sum_{i=1}^{N}\sum_{j=1}^{M} \frac{e^2 Z_j}{|\mathbf{r}_i - \mathbf{R}_j|} + \sum_{i<j} \frac{e^2}{|\mathbf{r}_i - \mathbf{r}_j|} + \sum_{i<j} \frac{e^2 Z_i Z_j}{|\mathbf{R}_i - \mathbf{R}_j|} \tag{2.2}$$

where W and $\Psi \equiv \Psi(\{\mathbf{R}_j\}, \{\mathbf{r}_i\})$ are the total energy and the eigenstate of the full system, respectively, m_e and M_j are the electronic and ionic masses, $-e$ and eZ_j are the electronic and ionic charges, $\mathbf{r}_i$ $(i = 1, ..., N)$ and $\mathbf{R}_j$ $(j = 1, ..., M)$ are the electronic and ionic coordinates. The first two terms in eq. 2.2 are the electronic and ionic kinetic energies, respectively, while the other terms represent the electrostatic interaction between electrons and ions, electrons and electrons, and ions and ions, respectively. Some approximation is needed to solve eq. 2.2 to find the ground state energy, W_0, and wavefunction, Ψ_0. The Born-Oppenheimer approximation allows to disentangle the ionic and electronic degrees of freedom. This approximation takes into account the fact that the ionic masses are much larger than the electronic one ($m_e/M_j < 10^{-3}$), and therefore the time scale of ionic dynamics is much longer than the electronic one. The ionic kinetic energy can thus be neglected when studying the electronic motion, and one can first

solve the problem of N interacting electrons, considering fixed ions acting as an external potential. The last term in eq. 2.2 becomes a constant at fixed ionic coordinates R_j , and one has to solve an electronic hamiltonian, where ionic positions are present as parameters. The approximation consists in writing the wavefunction $\Psi(\mathbf{R}, \mathbf{r})$ in the factorized form:

$$\Psi(\mathbf{R}, \mathbf{r}) = \Phi(\mathbf{R})\psi_{\mathbf{R}}(\mathbf{R}) \tag{2.3}$$

where the electronic wavefunction ψ depends parametrically on the ionic positions, and in neglecting the non-adiabatic terms which arise from the ionic kinetic operator acting on the electronic wavefunction. The Schrödinger equation 2.1 then factorizes into two separate equations for the ions and the electrons:

$$\left(-\sum_{j=1}^{M} \frac{\hbar^2}{2M_j} \nabla^2_{\mathbf{R}_j} + E(\mathbf{R}) \right) \Phi(\mathbf{R}) = \mathcal{E}\Phi(\mathbf{R}), \tag{2.4}$$

$$\left(-\sum_{i=1}^{N} \frac{\hbar^2}{2m_e} \nabla^2_{\mathbf{r}_i} + V_{el-el} + V_{el-I} + V_{I-I} \right) \psi_{\mathbf{R}}(\mathbf{r}) = E(\mathbf{R})\psi_{\mathbf{R}}(\mathbf{r}), \tag{2.5}$$

where we have abbreviated with V_{el-el},V_{el-I} and V_{I-I} the third, fourth, and fifth term in Eq. 2.2, respectively. Equations 2.4 and 2.5 are coupled via the term $E(\mathbf{R})$, which acts as a potential term in the ions hamiltonian and is determined by the solution of the electronic problem at fixed ionic positions. The stationary points of the effective potential $E(\mathbf{R})$ constitute what is known as the Born-Oppenheimer *potential energy surface* (PES), and determine the initial and final states of chemical reactions (local minima), as well as the transition states (saddle points) that separate the reactants from the products. All the efforts to solve and understand, by quantum mechanics first principles, the chemistry of reactions are about finding electronic energies and sampling in the best way the PES. Once the PES has been evaluated, Eq.2.4 can be solved either quantum-mechanically or

approximated by its classical counterpart $M_I\ddot{\mathbf{R}}_I = \mathbf{F}_I$, with the forces $\mathbf{F_I}$ given by the Hellmann-Feynman theorem:

$$\mathbf{F_I} = -\frac{\partial \mathbf{E}(\mathbf{R})}{\partial \mathbf{R_I}} = -\left\langle \psi_{\mathbf{R}}(\mathbf{r}) \left| \frac{\partial \mathbf{H_{el}}(\mathbf{R})}{\partial \mathbf{R_I}} \right| \psi_{\mathbf{R}}(\mathbf{r}) \right\rangle \tag{2.6}$$

where $H_{el}(\mathbf{R})$ is the operator on the left in Eq. 2.5. Thanks to the simplification provided by the Born-Oppenheimer separation of the degrees of freedom, the major difficulty is connected to the solution of the electronic equation 2.5.

This, however, is still a formidable task because of the electron-electron interaction: $\psi_{\mathbf{R}}(\mathbf{r})$ depends on the coordinates of all the electrons and cannot be factorized in single-particle contributions. A solution is provided by density-functional theory.

2.1.2 Density-Functional Theory

Density Functional Theory proposes a way to simplify the solution of the electronic problem, and the basic idea has been formulated by Hohenberg and Kohn in 1964 [17]. In the study of a many-electron problem, DFT avoids the calculation of the ground state wavefunction, which depends on the 3N electronic coordinates, and it shows that the ground state energy of a system of N interacting electrons can be expressed as a functional of the electron ground state density $n(\mathbf{r})$:

$$n(\mathbf{r}) = \langle \psi_0(\mathbf{r}_1, ..., \mathbf{r}_N) | \sum_{i=1}^{N} \delta(\mathbf{r} - \mathbf{r}_i) | \psi_0(\mathbf{r}_1, ..., \mathbf{r}_N) \rangle \tag{2.7}$$

where ψ_0 is the ground state wavefunction. Dealing with the density $n(\mathbf{r})$ is simpler than ψ_0, since it is a function only of the three spatial coordinates. Let's

write the electronic hamiltonian as:

$$H_{el} = T_e + V_{ee} + V_{ext} \tag{2.8}$$

where T_e is the electronic kinetic energy, V_{ee} is the electron-electron Coulomb interaction, and V_{ext} the external potential. Here we neglect the electrostatic interaction between ions, which is a constant at fixed ionic coordinates, and can be added to the total energy once the electronic problem is solved. Hohenberg and Kohn have demonstrated that not only the electron density in the ground state is uniquely determined by the external potential V_{ext}, but also the converse is true: the external potential V_{ext} is uniquely determined by $n(\mathbf{r})$, a part from an arbitrary constant potential. Since the external potential and N (which is simply the integral of the electronic density over the space) fully characterize the hamiltonian, it follows that $n(\mathbf{r})$ determines also the electron ground state wavefunction ψ_0. The total energy E of the electronic system can thus be written as:

$$E[n] = F[n] + \int v_{ext}(\mathbf{r})\, n(\mathbf{r})\, d\mathbf{r} \tag{2.9}$$

$F[n]$ is an universal functional of $n(\mathbf{r})$, which does not depend on the external potential, and it is given by:

$$F[n] = \langle \psi_0[n] | T + V_{ee} | \psi_0[n] \rangle \tag{2.10}$$

where $\psi_0[n]$ is the electron ground state wavefunction corresponding to $n(\mathbf{r})$. The last term in eq. 2.9, is the electronic interaction with the external potential V_{ext}, and its expression comes from the definition of the electron density in eq. 2.7,

and the fact that V_{ext} can be written as:

$$V_{ext}(\mathbf{r}_1, ..., \mathbf{r}_N) = \sum_i^N \int v_{ext}(\mathbf{r})\, \delta(\mathbf{r} - \mathbf{r}_i) d\mathbf{r} \tag{2.11}$$

$$v_{ext}(\mathbf{r}) = -\sum_j^M \frac{e^2 Z_j}{|\mathbf{r} - \mathbf{R}_j|}. \tag{2.12}$$

The ground state density of the system is the one which minimizes $E[n]$, and it can be shown that the minimum of $E[n]$ is the ground state energy of the system. According to this theory, once the functional $F[n]$ and the expression of the external potential are known, the exact ground state energy and density can be found. Unfortunately the exact expression of $F[n]$ is not known, and approximations are needed. A useful approximation has been proposed by Kohn and Sham in 1965 [18] , and their idea is that one can write $F[n]$ as a sum of well defined terms and a 'smaller' term which is unknown, not explicitly known, but which can be approximated. In particular:

$$F[n] = T_0[n] + E_H[n] + E_{ex}[n] \tag{2.13}$$

where $T_0[n]$ is the kinetic energy of an auxiliary system of non-interacting electrons, having the same density of the real system, $E_H[n]$ is the Hartree energy due to the classical interaction between electrons:

$$E_H[n] = \frac{e^2}{2} \int \frac{n(\mathbf{r}) n(\mathbf{r}')|}{|\mathbf{r} - \mathbf{r}'|}\, d\mathbf{r} d\mathbf{r}' \tag{2.14}$$

and $E_{xc}[n]$ is the exchange-correlation energy, which is the unknown part of $F[n]$. The density of the auxiliary system of non-interacting electrons can be written in terms of one-particle orbitals ϕ_i:

$$n(\mathbf{r}) = \sum_i^N |\phi_i(\mathbf{r})|^2 \tag{2.15}$$

The solution of the Schrödinger equation 2.5 for the system of N electrons is reduced to the minimization of the total energy functional $E[n]$ with respect to $n(\mathbf{r})$ under the condition $\int n(\mathbf{r})d\mathbf{r} = N$.This lead to the Kohn and Sham single particle equation:

$$\left(-\frac{\hbar^2}{2m_e}\nabla^2 + v_{ext}(\mathbf{r}) + V_H(\mathbf{r}) + \mu_{xc}(\mathbf{r})\right)\phi_i(\mathbf{r}) = \epsilon_i\phi_i(\mathbf{r}) \tag{2.16}$$

where:

$$V_H(\mathbf{r}) = e^2\int \frac{n(\mathbf{r}')}{|\mathbf{r}-\mathbf{r}'|}\,d\mathbf{r}' \tag{2.17}$$

$$\mu_{xc}(\mathbf{r}) = \frac{\delta E_{ex}[n]}{\delta n(\mathbf{r})}, \tag{2.18}$$

The application of DFT to a real system requires an approximation for the exchange-correlation energy $E_{xc}[n]$ and its functional derivative $\mu_{xc}(\mathbf{r})$. The simplest approximation is the so called local-density approximation (LDA) which assumes that the exchange-correlation energy per particle is locally equal to the one of an ideal uniform electron gas with the density equal to the density of the real system in the point considered:

$$E_{xc}^{LDA}[n(\mathbf{r})] = \int \epsilon_{xc}^{hom}[n(\mathbf{r})]\,n(\mathbf{r})\,d\mathbf{r} \tag{2.19}$$

where $\epsilon_{xc}^{hom}[n(\mathbf{r})]$ is the exchange-correlation energy per particle of the uniform electron gas. The exchange-correlation potential $\mu_{xc}(\mathbf{r})$ as defined in eq. 2.18 becomes:

$$\mu_{xc}^{LDA}(\mathbf{r}) = \frac{\delta E_{xc}^{LDA}[n(\mathbf{r})]}{\delta n(\mathbf{r})} = \frac{d}{dn}\left(\epsilon_{xc}^{hom}(n)\,n\right)|_{n=n(\mathbf{r})} \tag{2.20}$$

The use of LDA approximation for the exchange-correlation functional gives good results for structural properties of systems where the electron density changes slowly, and to describe ionic, covalent and metallic bonds. However, binding energies are usually overestimated by LDA, in particular for systems where weaker

bonds are present. Another class of approximations for the exchange-correlation functional is the Generalized Gradient Approximation (GGA), where it is assumed that E_{xc} depends not only on the electron density, but also on the local gradient of the electron density:

$$E_{xc}^{GGA}[n, |\nabla n|] = \int F_{xc}[n, |\nabla n|]\, d\mathbf{r} \tag{2.21}$$

2.2 Thermally activated processes and Nudged Elastic Band

DFT is a theory of the electronic ground state for a given atomic configurations which is not necessarily the ground state for the ionic subsystem. Therefore, the properties of the system that is far from equilibrium can also be studied under the constraint imposed by the adiabatic approximation . This is typically done in the molecular dynamics simulations (see for example reference [19]). However, the activated processes in which the system undergoes a transition from one local minimum to another one across an energy barrier are extremely difficult to study by means of standard molecular dynamics. Processes with a relatively low activation energy of 0.5 eV would require years of computer time to simulate classical trajectory of the system in order for a single transition event to be expected to occur (Fig.2.1).

This problem can be overcome and satisfactory estimates of the transition rates can be obtained by using the transition state theory (TST) [20]. In addition to the adiabatic approximation TST relies on two assumptions: (i) the transition rates are slow enough and a Boltzmann distribution describes the reactant state; and (ii) the initial and final states can be separated in the configurational space

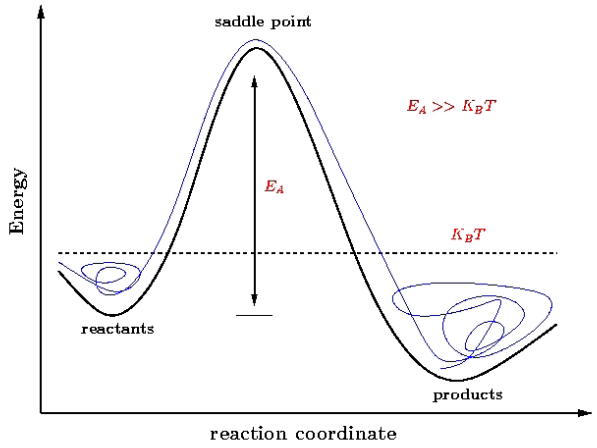

Figure 2.1: *A one dimensional picture of a thermally activated process. For low temperatures the trajectory is concentrated near initial and final state and the transition is a rare event.*

by a D-1 dimensional surface (D is the number of degrees of freedom) in such a way that the trajectory going from one state to the other crosses this surface only once. Since the temperatures range of interest, when considering condensed matter systems, lays typically far below the melting temperature, the harmonic approximation to TST (hTST) can be used for studying diffusion or reactions at crystal surfaces. This simplifies the problem which becomes that of finding the saddle point (transition state) along the minimal energy path (MEP) connecting the two states (initial and final). The rate constant for the transition can be obtained from the energy and the frequency of the normal modes of the initial and transition state [21].

$$k^{hTST} = \frac{\prod_i^{3N} \nu_i^{init}}{\prod_i^{3N-1} \nu_i^*} e^{\frac{-(E-E^{init})}{k_B T}}, \tag{2.22}$$

where E* and E^{init} are the energies of the saddle point and initial state, respec-

tively. The ν_i appearing in the prefactor that multiplies the exponential term in Eq.2.22 are the corresponding normal mode frequencies. In the cases where transition occurs along one of the normal modes of the initial states the whole prefactor could be approximated with the frequency of that mode solely. Moreover, in the solid state systems the frequencies are of the order of $10^{12} \div 10^{13}\, Hz$. This value is often used for rough estimations of the rate constants.

The MEP often has one or more minima in addition to those of the initial and final states which correspond to the (meta)stable intermediate configurations. Therefore, along the MEP there are also several saddle points, one between each pair of neighboring minima. If a Boltzmann population is reached for the intermediate configurations the overall rate is then determined by the highest transition state.

Various methods are in use for calculating MEPs and finding the transition states. One of the most efficient is the nudged elastic band (NEB) method [22]. It has been widely used together with hTST. The idea is to discretize the initial path (guess) in the configurational space of the system between the two end points and to relax each of the resulting configurations only in the directions perpendicular to the path. This is done by putting all components of the forces that lay along the path to zero and performing standard minimization techniques. However, the definition of the tangent as well as the number of points used for discretization is crucial (see more about this in reference [22]). Since the relaxation of each point depends on the tangent and therefore on the configurations of other points, the relaxation towards the MEP is performed simultaneously for all points along the path. To prevent grouping of the images and other types of path instabilities the spring forces are added between neighboring configurations making an elastic

band in the configurational space. The tangential components of the spring force are used to control the spacing between images (normal components are set equal to zero). Calculations of the energies and forces of different configurations are typically done using DFT methods.

The Climbing Image Nudged Elastic Band method (CI-NEB) [21] can then be used to find the saddle points along the path. After the initial path has approached closer to the MEP the configurations that have to 'climb' are detached from the springs and allowed to relax also in the tangential direction. This relaxation is done by inverting the tangential components of the forces. In this way the chosen configuration climbs to the point with the zero force, which is a minimum in all directions perpendicular to the path and a maximum in the tangential direction, the first order saddle point or the transition state.

2.2.1 Computational details

All calculations are performed in the framework of Density-Functional Theory, as implemented in the `Quantum ESPRESSO` distribution (`http://www.quantum-espresso.org`)[16]. We used the pseudopotential method with ultrasoft pseudopotentials [23]. The following pseudopotential (availables on the page `http://www.quantum-espresso.org/pseudo.php`) have been used: `C.pbe-rrkjus.UPF, H.pbe-rrkjus.UPF, O.pbe-rrkjus.UPF, Ni.pbe-nd-rrkjus.UPF` for GGA, and `C.pz-rrkjus.UPF, H.pz-rrkjus.UPF, O.pz-rrkjus.UPF, Ni.pz-nd-rrkjus.UPF` for LDA. The calculation are performed using different parallel machines: BCX and SP6 clusters at CINECA, and Matrix cluster at CASPUR. All molecular graphics shown in this thesis were produced by the `XCRYSDEN` graphical package [24].

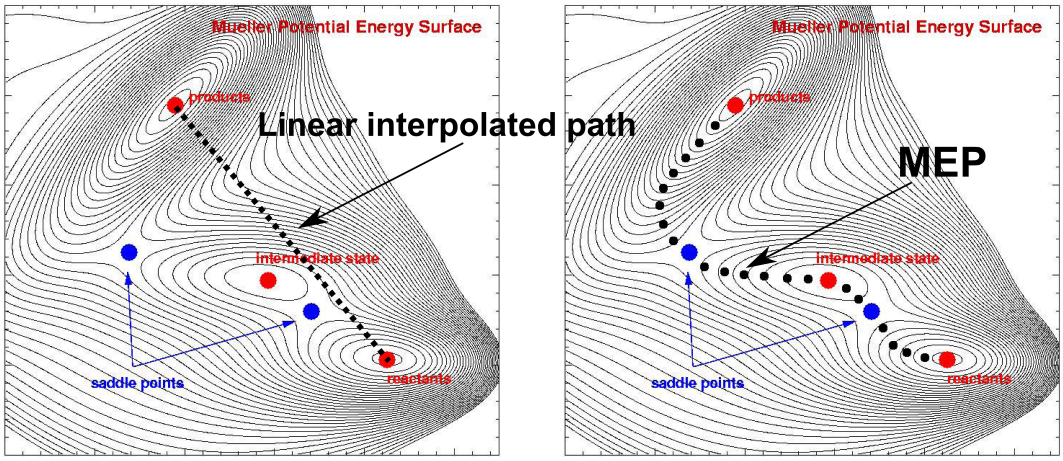

Figure 2.2: *An example of a potential surface. We are looking for saddle points (blue spots), given an initial and final states (red spots). In this case the surface has also an intermediate minimum. In the second picture we have depicted the final result of a working algorithm. The sample well represents the MEP and we have images at each of the key points.*

Chapter 3

Gas phase CO_2 molecule and Ni(110) surface

Before approaching the system 'surface+adsorbe' it is important to test our calculations on its constituents, and compare them with existing in literature. In this chapter we present the result on the free CO_2 molecule and the clean Ni(110) surface.

3.1 Gas phase carbon dioxide molecule

As we will see in Chap. 4, the adsorbed CO_2 on Ni(110) is charged and bent; for this reason we studied in gas phase not only the neutral, closed shell, linear molecule, but also the charged molecule CO_2^-. The simulation of charged systems with a code like PWscf that uses periodic boundary conditions requires that a compensating jellium background is inserted to remove divergences. Moreover a charged-isolated system requires a correction to the energy to compensate spurious interactions induced by the periodic boundary condition: we used the

Makov-Payne correction [25]. The simulation cell was a simple cube and the choice of its side was carefully tested: indeed charged molecules in periodic systems converge slower. For this reason we performed the convergence tests on the charged molecule, obtaining a satisfying convergence for a 7 Å side cubic cell.

A cubic cell is used and the geometrical convergence of the CO_2^- molecule was achieved with a side of 7 Å . We used the spin-polarized σ-GGA for the exchange-correlation functional in the Perdew-Burke-Ernzerhof implementation [26], the valence electronic wave functions were expanded by a plane wave basis set with a kinetic energy cutoff of 24 Ry (convergence tests with 32 Ry), while Brillouin zone was sampled using the Baldereschi point[1] [27].

For neutral linear CO_2 calculations give a distance C-O of 1.17 Å , while in the charged molecule this distance increase up to 1.24 Å and the angle O-C-O is 137.2°. Löwdin population analysis [28], by projecting Bloch wave functions onto linear combinations of spin-resolved atomic orbitals, was used to obtain information about the atomic charges. For comparison, also the charged molecule with a constrained linear geometry and the neutral molecule with the CO_2^- geometry were studied. Table 3.1 shows the atomic charges for the neutral, linear, gas phase free standing CO_2, and related variations for the other three cases. We can see that the extra charge distributes almost homogeneously on linear charged CO_2 , while in bent CO_2^- the bending is accompanied by a the charge on C atom, especially on 2s orbital. The localization of the extra charge on C atom is accompanied with the spin polarization (1.0 μ_B) showed in Fig. 3.1.

[1]For a cubic cell $\mathbf{k}^* \equiv \frac{\pi}{a}\left(\frac{1}{2}, \frac{1}{2}, \frac{1}{2}\right)$.

Molecule	Atom	Tot	2s	2p
CO_2	O	**-0.30**	+0.34	-0.64
	C	**+0.60**	+1.18	-0.58
CO_2^-	O	-0.28	-0.06	-0.22
	C	-0.44	-0.30	-0.14
neutral bent CO_2	O	+0.03	-0.06	+0.09
	C	-0.06	-0.10	+0.06
linear CO_2^-	O	-0.36	-0.10	-0.26
	C	-0.28	-0.12	-0.16

Table 3.1: *Atomic charge (in units of $|e|$) of free standing CO_2, and related variation in CO_2^-, neutral bent CO_2 (in the CO_2^- geometry) and charged linear CO_2 .*

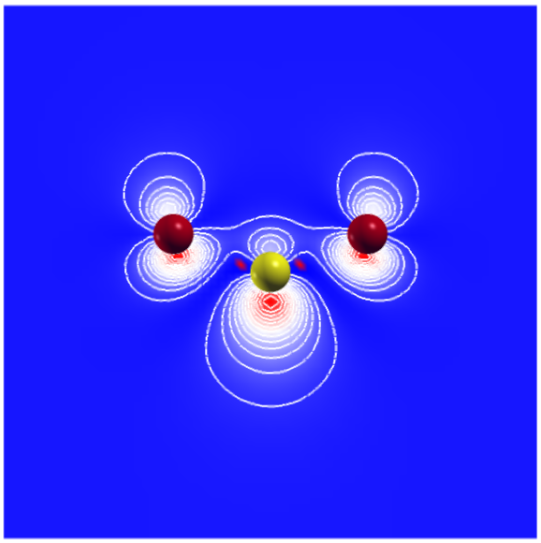

Figure 3.1: *Spin polarization ($\rho(\downarrow) - \rho(\uparrow)$) of CO_2^-.*

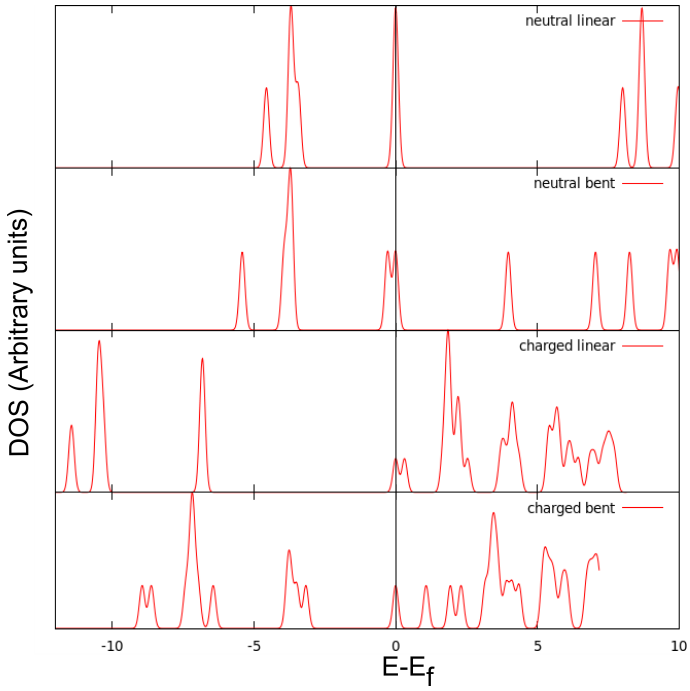

Figure 3.2: *DOS density of states of free CO_2 molecule, in neutral linear configuration, neutral bent configuration (with the fixed geometry of the charged bent configuration), charged linear configuration (with the fixed geometry of the neutral linear configuration) and charged bent configuration. The origin is fixed to the HOMO.*

Figure 3.2 shows the density of state of the four systems. From PDOS[2] analysis it results that, in the case of neutral linear CO_2 , the HOMO is projected on 2p orbitals of O atoms ($1\pi_g$), while the LUMO is a combination of 2s and 2p of the carbon and 2p of the oxygen; the energy difference HOMO-LUMO is 4.3 eV. The bending in the neutral bent molecule splits the HOMO and lowers

[2]The projected DOS (PDOS) onto the atomic wave-functions ϕ_s^{at} is:

$$n_s(E) = \int_{BZ} d\mathbf{k} \ |\langle \psi_{\mathbf{k}} | \phi_s^{at} \rangle|^2 \ \delta(E(\mathbf{k}) - E) \tag{3.1}$$

were $\psi_{\mathbf{k}}$ is the solid wave-function at wave-vector $\mathbf{k}$.

the difference HOMO-LUMO to 3.9 eV. In the charged linear CO_2 only the 2s orbital of carbon atom contributes to the HOMO, while in the charged bent CO_2^- HOMO and LUMO have identical character with oxygen 2p and carbon 2s and 2p components, but with the opposite spin with a difference of by 1.05 eV.

3.2 Ni(110) surface

Ultrasoft pseudopotentials and spin generalized gradient approximation (σ-GGA) for the exchange and correlation (XC)term in the Perdew-Burke-Ernzerhof [26] implementation have been used for Ni. We performed for comparison some tests with the local density approximation (LDA)[29]. The valence electronic wave functions were expanded by a plane wave basis set with a kinetic energy cutoff of 24 Ry (convergence tests with 32 Ry). The Brillouin zone integration for bulk Ni(fcc) was carried out with smearing techniques using a $12 \times 12 \times 12$ k-point mesh and corresponding meshes for supercells [30, 31] (energy broadening of 0.01 Ry). For bulk Ni, the GGA equilibrium lattice constant is equal to 3.52 Å , the bulk modulus 1.92 Mbar, and the magnetic moment 0.59 μ_B, in standard good agreement with the corresponding experimental values of 3.52 Å , 1.86 Mbar, and 0.61 μ_B, respectively [32]. LDA calculations give instead 3.42 Å for the lattice constant and 2.50 Mbar for the bulk modulus, thus giving an overbinding effect, as often occurs. The magnetic moment obtained by LDA, $\mu(B) = 0.57\mu_B$, is however in rather good agreement with experiments. The metal surface is modeled by a two-dimensional slab in a three dimensional supercell generated by introducing a vacuum space of 15 Å in the normal direction to the surface. Table 3.2 shows the energetic and geometric properties for a slab of 5, 7 and 9 layers of Ni(110). Comparing the results of 5 layers with those of 7 and 9 layers, no

substantial differences can be found, neither in terms of geometry nor of magnetic properties. Furthermore, it has been found in Ref. [33] that even in case of CO adsorption on Ni(110) surface, where the adsorbed CO has much stronger interaction with the surface than CO_2 , effects related to surface and bonding extend only up to the subsurface layer, and the third one is almost bulklike. Therefore we adopted slabs with 5 Ni layers, and constructed the supercells keeping the third layer fixed. Figure 3.3 shows the density of states projected Ni atoms of first, second and third layers for the Ni(110).

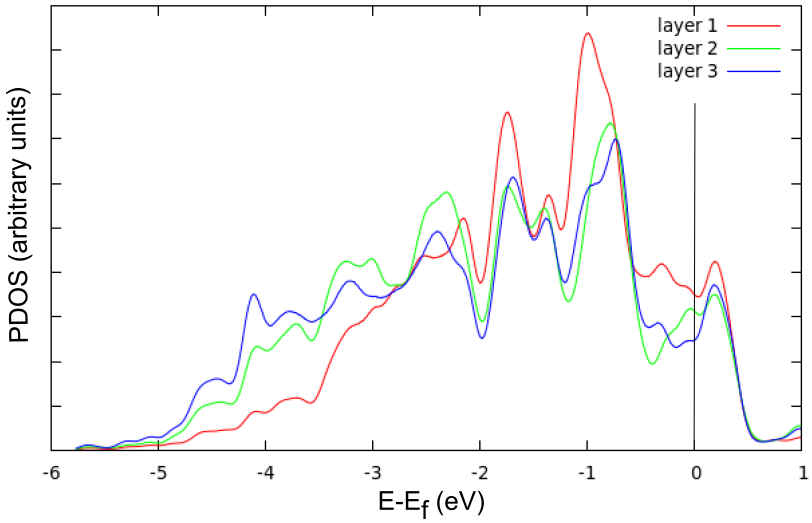

Figure 3.3: *Layer projected DOS for the three different layers in a 5-layer Ni(110) slab.*

Table 3.2: *Variation of the interlayer distance Δd_{ij}, surface formation energy σ per surface unit cell and atomic magnetic moments of the clean Ni(110) surface for 5, 7 and 9 Ni layers (L), after optimization of the atomic position using σ-GGA*

	5L	7L	9L[a]	Expt.
$\Delta d_{12}(\%)$	-10.7	-10.1	-10.4	-9.0[b]
$\Delta d_{23}(\%)$	+3.5	+3.6	+3.1	+3.5[b]
$\Delta d_{34}(\%)$		-0.4	0.0	-0.5[c]
$\sigma(eV)$	1.18	1.22	1.24	
$\mu_{(B)}(\mu_B)$	0.61	0.61	0.61	0.61[d]
$\mu_{(S-3)}(\mu_B)$		0.60	0.62	
$\mu_{(S-2)}(\mu_B)$	0.66	0.63	0.62	
$\mu_{(S-1)}(\mu_B)$	0.60	0.62	0.63	
$\mu_{(S)}(\mu_B)$	0.75	0.73	0.75	
$\Delta\mu_{S-B}(\%)$	+23	+20	+23	

The percentage variation of the interlayer distance is computed with respect to the nickel bulk interlayer spacing. The magnetic moment $\mu_{(B)}$ is for a bulk Ni atom and $\mu_{(S-i)}$ is for a Ni atom in the layer i from the surface (i=0 corresponds to the surface). Surface-induced enhancement ($\Delta\mu_{S-B}$) of the magnetization is calculated from $\mu_{(B)}$ and $\mu_{(S)}$.

[a][33],[b][34], [c][35],[d][32]

Chapter 4

CO_2 adsorption on Ni(110)

In this chapter we present the study of the adsorption of carbon dioxide molecule on Ni(110) surface. Energetic end geometric properties are firstly analyzed, followed by the study of electronic structure, namely the analysis of the atomic charge and of the density of states. In the second part of the chapter the first LT-STM experimental images of CO_2 on Ni(110) are compared with the simulated ones, giving the direct confirmation of the predicted adsorption configurations. The chapter ends with the analysis of vibrational properties and the study of the most important reaction barriers. Through this chapter we compare our theoretical results with the experiments performed at TASC laboratory. The main results presented in this chapter were published in Physical Review B [36].

4.1 Technicalities

Adsorbates on surfaces can be modeled using two different setups:

1. A periodically repeated supercell containing the slab with the adsorbate on one side of the slab(C_1 space symmetry. A dipole can be therefore

induced and in principle we must introduce correction to compensate the dipole interactions between unit cells through the vacuum regions. The uppermost metal layer are allowed to relax and others are fixed at optimized bulk geometry.

2. Adsorbates cover both sides of the slab geometry (made with an odd number of layers) in a S_2 space group symmetry, in general.The central layer is keept fix. This geometry avoids dipole interaction between unit cells.

Provided that numerical convergence is reached, the two setups are equivalent. We focus on the former. The study of isolated adsorbed molecule was performed using supercells with a
3×3 in-plane periodicity and one CO_2 molecule, corresponding to a coverage of $\frac{1}{9}$ ML. Both larger and smaller supercells were used to estimate the strength of lateral interaction between repeated images of adsorbed molecules. Most of the calculations were performed with a Ni slab thickness of five layers and a vacuum space of 15 Å. We checked that a five layer Ni slab plus a vacuum space of three times the slab thickness is enough to almost entirely screen the fictitious electric field in the supercell due to the asymmetry of the finite system in the direction perpendicular to the surface, so that no dipole correction was needed. The valence electronic wave functions were expanded by a plane wave basis set with a kinetic energy cutoff of 24 Ry (convergence tests with 32 Ry) as in the Chap.3.2 and Chap.3, while Brillouin zone was sampled with a $4 \times 3 \times 1$ k-point mesh (that is (corresponding to sample with a $12 \times 12 \times 12$ k-point mesh for the primitive cell of the bulk Ni), with a of 0.01 Ry using the Methfessel-Paxton technique.

We attribute to the adsorption energies calculated with a five-layer thick supercell a numerical uncertainty of ± 0.1 eV mainly due to the thickness of the slab. However differences between the energies energy of different adsorption configurations in five-layer thick supercell are affected by a numerical uncertainty of only ≈ 0.02 eV. The latter is also the uncertainty due to the other technical ingredients such as k-point mesh.

We used the σ-GGA for the exchange-correlation functional in the Perdew-Burke-Ernzerhof implementation. To take into account the van der Waals contribution that can be important for weakly adsorbed molecule, the calculations were also performed using a semi-empirical addition of dispersive forces to conventional density functionals in the framework of the DFT-D approach [37] , implemented in the QE suite [16].

4.2 Energetics and geometry

Several adsorption configurations were considered, starting from those with C_{2v} and C_s symmetries on high symmetry sites suggested in literature [2] and including others obtained by relaxing the symmetry constraints. To find equilibrium geometries, we fixed the central layer of the Ni slab at the bulk equilibrium positions and we performed an unconstrained optimization of all the other atomic positions, allowing them to relax until atomic forces were smaller than 1 mRy a.u^{-1} and the total energy was minimized.

Our calculations predict the existence of four stable chemisorbed configurations shown in fig.4.1: the 'hollow-up' (HU), the 'hollow-up symmetric' (HU-s) and the 'hollow-symmetric' (HS), both positioned at hollow sites, in addition to 'short-bridge' (SB) [3].

All the chemisorbed configurations are characterized by a CO_2 molecule bent, negatively charged, bond with the Ni surface mainly through the C atom. This is at variance with what proposed in past literature [1, 2] i.e., a molecule bonded to the metallic surface mainly via oxygen atom, in analogy with the well known chemisorbed configuration of formate (HCOO). More recent calculation [6] have however suggested that the most stable geometry is not symmetric.

The HS and the SB configurations are compatible with a C_{2v} symmetry with the molecular plane perpendicular to the surface and parallel to the [001] direction for the HS and parallel to the $[1\bar{1}0]$ direction for the SB.

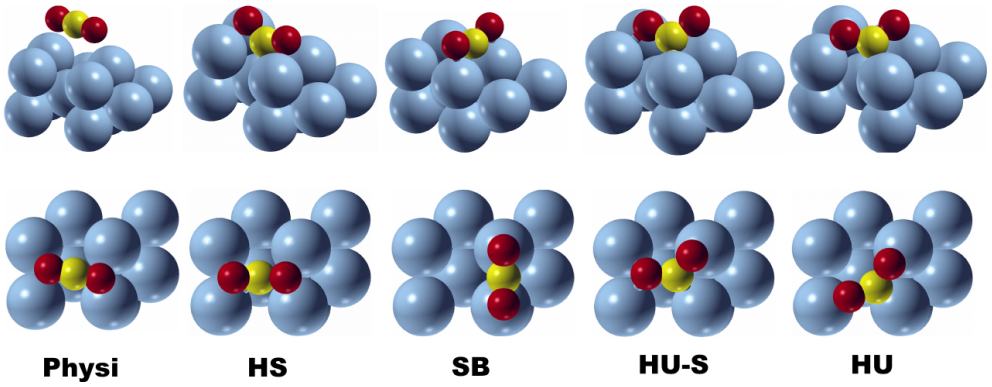

Figure 4.1: *Models of four differnt chemisorbed CO_2 configurations.A possible physisorbed configuration (left) is also shown for comparison, but it is only representative of many equivalent ones. Only first three surface Ni layers are shown.*

The binding geometries of CO_2 with Ni in the HU and HU-s configurations have common features. In the HU configuration the molecule forms a strong bond between C and one surface Ni atom and weak O bonds with two Ni neighbors, with the molecular plane inclined by about 30° with respect to the Ni surface normal. The HU-s is very similar, but with one of the two C-O bonds in a more symmetric position, with the oxygen atom coordinated with two surface

Table 4.1: *Calculated DFT-D geometries for the adsorption states of CO_2 on Ni(110). (Columns from left to right report: distance between the carbon atom and the nearest Ni atom; distance between the carbon atom and the surface Ni plane) (z_C); C−O bond length(s) (d_{C-O}); O−C−O angle (α_{O-C-O}).*

States	d_{C-Ni}(Å)	z_C(Å)	d_{C-O}(Å)	α_{O-C-O}(°)
HU	1.91	1.37	1.28	126.0
HU-s	1.93	1.23	1.32–1.27 [1]	121.7
SB	2.06	1.73	1.23	140.7
HS	1.90	0.95	1.30	121.9
phys.		3.45 (2.76)	1.17	179.9

[1]The two oxygen atoms are non-equivalent

Ni atoms. In all four configurations, the atoms are coordinated with surface Ni atoms except in the HS configuration, in which the carbon atom is coordinated with a subsurface atom, with a distance of 1.9Å (tab.4.1).

Besides the four chemisorbed configurations, using the DFT-D approach, we also found a physisorbed configuration: the CO_2 molecule remains linear, parallel to the surface, undistorted at a distance of 2.76 Å from the surface.

The adsorption energies for the different configurations are calculated as

$$E_{ads} = -(E(\mathrm{CO_2/Ni}_{slab}) - E(\mathrm{CO_2}) - E(\mathrm{Ni}_{slab})) \tag{4.1}$$

and are shown in tab. 4.2. With this definition, a positive energy indicates adsorption. The results indicate that CO_2 adsorbs weakly on Ni(110) and the inclusion of dispersion force is therefore important. We also performed simulations with GGA and LDA (without dispersive forces correction) for comparison. The GGA usually underestimates adsorption energies. The DFT-D correction

gives for the chemisorbed configurations systematically larger adsorption energies by about 0.4 eV with respect to the values obtained with standard GGA. Test calculations made using both LDA and GGA indicate that the DFT-D estimates are almost in between GGA and LDA results and give the same relative stability for the chemisorbed configurations, except for the HS configuration that results the most stable one in LDA.

DFT-D results are instead clearly different from GGA for the weakly bound, metastable state representing a physisorbed configuration: the DFT-D calculations provide a clear indication of the existence of a local energy minimum characterized by an adsorption energy of about 0.3 eV (instead of the 0.06 eV within standard GGA) and a distance from the surface of 2.76Å (instead of about 4Å in GGA). To deeply understand the difference of the GGA results with and without the Van der Waals correction we plotted the interaction energy [1] CO_2 -Ni_{slab} for different distances of carbon atom from Ni surface: we fix the (x,y) coordinates of C atom as in the HS configuration and we consider different z values, relaxing the two O atom and the first two surface Ni layers. We can see that only the DFT-D semiempirical correction indicates a clear minimum (see fig. 4.2).

Regarding the chemisorption energies, we have pointed out that the numerical uncertainty on the relative energies (due to supercell size, slab and vacuum thickness, kinetic energy cutoff, special k-point set for Brillouin zone sampling) is

[1] The interaction energy is defined as:

$$E_{int}(d) = E(d)[\mathrm{CO_2} + \mathrm{Ni}(110)_{slab}] - E[\mathrm{CO_2}] - E[\mathrm{Ni}(110)_{slab}] \tag{4.2}$$

where $E(d)[\mathrm{CO_2} + \mathrm{Ni}(110)_{slab}]$ is the total energy of the system $\mathrm{CO_2} + \mathrm{Ni}(110)_{slab}$ at distance d of carbon atom from the surface.

States	E_{ads}^{GGA}(eV)	E_{ads}^{LDA}(eV)	$\boldsymbol{E_{ads}^{DFT-D}}$(eV)
HU	0.24	1.52	**0.66**
HU-s	0.19	1.54	**0.60**
SB	0.17	1.14	**0.52**
HS	0.09	1.57	**0.50**
phys.	0.06		**0.29**

Table 4.2: *DFT adsorption energies for CO_2 adsorbed on Ni(110) with a coverage of $\frac{1}{6}$ ML, obtained with different approximations for exchange-correlation functional and with (last column) and without (first two columns) dispersion forces correction.*

of the order of 0.02 eV. However the uncertainty due to physical approximations (exchange-correlation functional) could be larger and comparable with the energy difference between different adsorption configurations, therefore the resulting picture is a set of four almost equivalent adsorption configurations lying around an average value of adsorption energy of 0.57 eV within an energy range of 0.15 eV (i.e., about 20 %).

To check the dependence of the energy on the coverage (i.e. to estimate the lateral interactions) we calculated the adsorption energy of the HS configuration with a coverage of $\frac{1}{4}$ ML and $\frac{1}{2}$ ML (fig. 4.3) and obtained respectively 0.50 eV and 0.15 eV, yielding a large repulsion between the adsorbed molecules in the latter case. This is consistent with the experimentally observed saturation coverage of about $\frac{1}{3}$ ML (Fig. 4.5). For this reason we studied the coexistence of $\frac{1}{4}$ ML of HS species with $\frac{1}{4}$ ML of physisorbed CO_2 arranged as in fig. 4.4. The calculation gives a physisorption energy of 0.27 eV. This suggests that there is

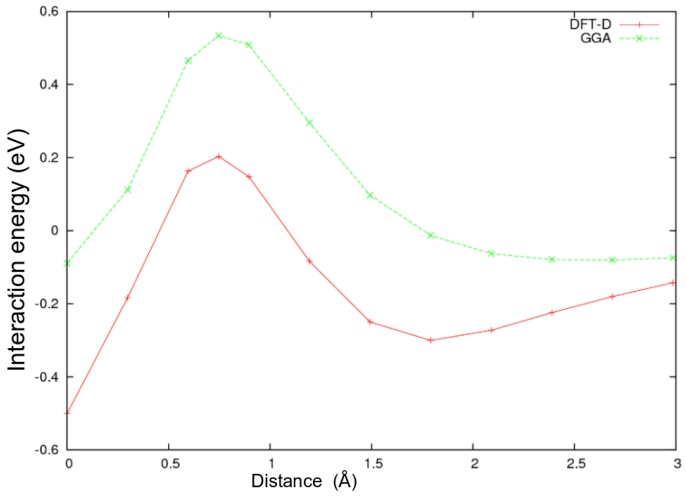

Figure 4.2: *CO_2-Ni(110) Interaction energy for different C atom distances from HS chemisorption position with GGA and DFT-D functionals. The zero energy corresponds to infinite separation.*

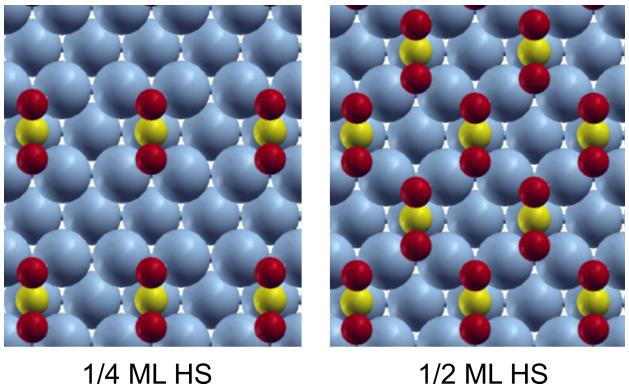

Figure 4.3: *Models for adsorbed CO_2 in HS geometry with coverage of 1/4 ML and 1/2 ML.*

almost no interaction between the molecules (cfr. tab. 4.2) and that chemisorbed CO_2 molecule exceeding a coverage of about $\frac{1}{4}$ ML are physisorbed.

These conclusions are in good agreement with the TPD experimental results

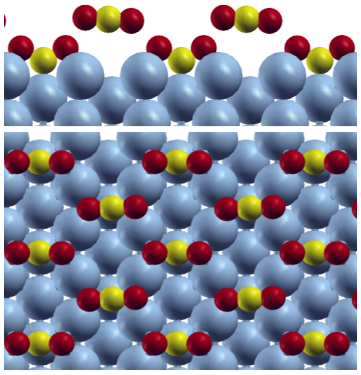

Figure 4.4: *Top and side view of arrangement of 1/4 ML HS and 1/4 ML of physisorbed CO_2 used for simulations.*

[3]. Fig. 4.5 shows the mass 44 TPD spectra obtained as a function of the initial CO_2 exposure at 90 K and with a linear temperature ramp of 1.5 K/s. For exposures above 0.3 L (1 L=10^{-6} Torr s), two distinct mass 44 peaks are observed at 100 and 220 K, respectively. The low-temperature feature is due to the desorption of the CO_2 physisorbed multilayer, while the higher temperature peak is related to chemisorbed CO_2. Desorption from the low-temperature state takes place immediately with heating, thus indicating that its population is limited by the adsorption temperature. Chemisorbed CO_2 , on the contrary, is stable on the surface up to 220 K. For exposures lower than 0.3 L, physisorbed CO_2 is absent. Assuming a first order desorption process[38] and a trial standard preexponential factor of $10^{13}s^{-1}$, the estimated desorption energies from the features at 222K and 100K are 0.60 ± 0.15 eV and 0.26 ± 0.05 eV for the chemisorbed and physisorbed multilayer species. We must caution the reader that the experimental desorption energy cannot be immediately compared with the calculated adsorption energy: if the adsorption process is activated (i.e. if there is an energy barrier for a molecule to approach the surface from the gas phase and bind to

it), the desorption energy is the sum of the adsorption and the activation barrier. As we will see in the Sec. 4.6 (Fig. 4.13), in DFT-D corrected DFT the CO_2 adsorption is not activated, so we can directly compare experimental desorption energies with calculated adsorption energies.

The peak at 220K is therefore compatible with our calculated chemisorption energies, while the low temperature peak can be ascribed to physisorbed CO_2 floating over a saturated layer of chemisorbed CO_2 .

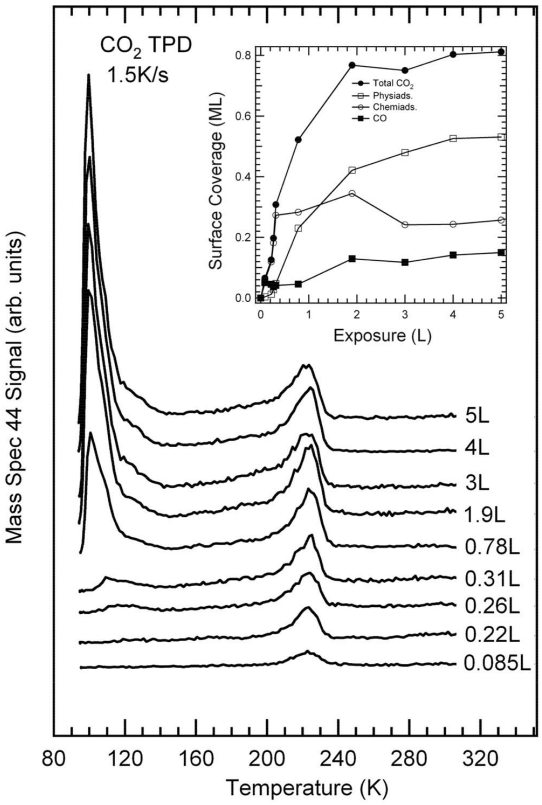

Figure 4.5: *Experimental TPD spectra obtained on Ni(110) as a function of the initial CO_2 exposure at 90 K. In the inset, a plot of the total and relative CO_2 desorbing coverage is shown, together with a quantification of the formed CO. The latter concentration is calculated via a cross-link between the TPD and the XPS data [3]*

4.3 Electronic structure

4.3.1 Charge

Löwdin population analysis [28], by projecting Bloch wave functions onto linear combinations of spin-resolved atomic orbitals, was used to obtain information about the atomic charges. All chemisorbed geometries are characterized by a sizable electron transfer from surface to CO_2 , as it can be estimated by calculating the atomic Löwdin charges (see Table 4.3): the total charge transfers from the substrate to the molecule are 0.85, 0.97, 0.58 and 1.00 electrons for the HU, HU-s, SB and HS configurations, respectively, as obtained by DFT-D for 1/9 ML coverage, with an estimated error of $\pm$ 0.05 electrons due to the projection procedure (the error being obtained from the calculated spilling parameter [39]).

The net atomic charge is mainly localized on the oxygen atoms: in the HS (fig. 4.6), for example there is no net charge on the carbon atom, while a charge of 0.5 $|e|$ is localized on each oxygen atom, thus resulting in a net dipole due to the bent geometry.

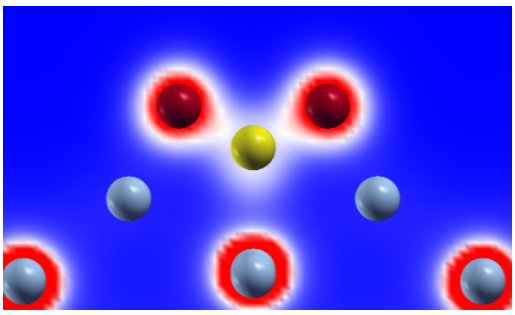

Figure 4.6: *Charge density projected onto CO_2 molecular plane of HS configuration.*

Extra electrons on the adsorbed molecule come from the Ni atoms close to

	GGA				**DFT-D**			
Configuration	**C**	O_1	O_2	TOT	**C**	O_1	O_2	TOT
CO_2	0.58	-0.29	-0.29	0.00	0.60	-0.30	-0.30	0.00
HU	-0.53	-0.21	-0.19	-0.93	-0.51	-0.18	-0.16	-0.85
HU-S	-0.55	-0.27	-0.15	-0.97	-0.57	-0.26	-0.14	-0.97
SB	-0.41	-0.11	-0.11	-0.63	-0.40	-0.09	-0.09	-0.58
HS	-0.58	-0.21	-0.21	-1.00	-0.60	-0.20	-0.20	-1.00

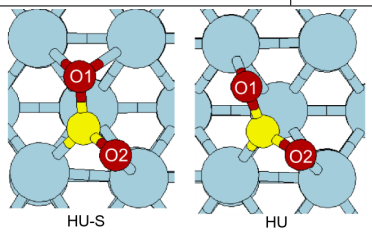

Table 4.3: *Atomic charges (in units of |e|): in the isolated, free standing, neutral and linear CO_2 molecule (first row) and related variations in the adsorbed geometries. The first row for DFT-D corresponds to the first one of Tab.3.1.*

CO_2: Figure 4.7 shows the differential charge density. Charge rearrangement can be clearly seen from the differential plot of the charge density, which is defined as

$$\Delta\rho = \rho(\mathrm{CO_2/Ni}) - \rho(\mathrm{Ni}) - \rho(\mathrm{CO_2}) \tag{4.3}$$

were $\rho(\mathrm{CO_2/Ni})$ is the charge density of HS adsorbed configuration while $\rho(\mathrm{Ni})$ and $\rho(\mathrm{CO_2})$ are calculated with the geometries fixed corresponding to the system slab+adsorbate. It can be seen that the electronic distribution changes mostly around the Ni atoms in the top layer, and in the sublayer for the HS configuration. There is a considerable charge accumulation (positive differential charge density, red lobes) between C and the attached Ni atom, which clearly indicates a C-Ni bonding. At variance, no additional electronic charge is found between O atoms and corresponding Ni atoms, thus indicating a much weaker interaction between them. The transferred charge on C atom in HS (0.6 $|e|$) is shared in equal amount between the 2s and 2p orbital, while on the oxygen atoms the transferred charge is only accumulated on the 2p orbitals.

4.3.2 Density of states

To explain the electronic structures of the chemisorbed CO_2, the density of state projected on the atomic wave-functions [2] of CO_2 atoms was calculated. As shown in Figure 4.8 and Fig. 4.9 with additional details of atomic orbitals resolution, the highest occupied molecular orbital (HOMO) of free (neutral linear) CO_2 is

[2]The projected DOS onto the atomic wave-functions ϕ_s^{at} is:

$$n_s(E) = \int_{BZ} d\mathbf{k}\ |\langle\psi_{\mathbf{k}}|\phi_s^{at}\rangle|^2\ \delta(E(\mathbf{k}) - E) \tag{4.4}$$

were $\psi_{\mathbf{k}}$ is the solid wave-function at wave-vector $\mathbf{k}$.

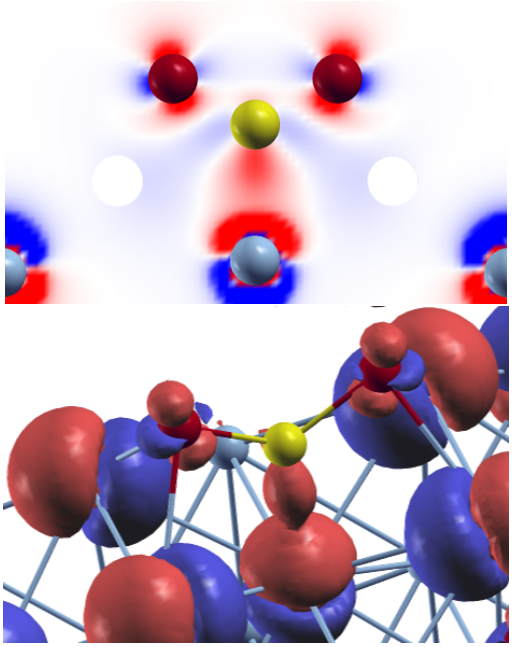

Figure 4.7: *Upper panel: Differential Charge density projected onto CO_2 molecular plane of HS configuration. Lower panel: isosurface of differential charge density for HS configuration. Red in differential charge density denotes excess of electron density and blue denotes lack of electron density*

$1\pi_g$, which is situated on oxygen atoms (Fig. 4.9, upper panel), while the lowest unoccupied molecular orbital (LUMO) is $2\pi_u$, which is the antibonding orbital of CO_2 situated on the carbon atom and two oxygen atoms (Fig. 4.9, lower panel). In the chemisorbed CO_2 , atomic energy levels shift downward (Fig. 4.8 (HS)) which corresponds to the binding of CO_2 with the nickel surface. As a consequence of charge transfer (see 4.3.1), the antibonding $2\pi_u$ orbital shifts below the Fermi level for the chemisorbed species and the intensity is also lowered considerably as compared with free CO_2 . As we can see in Fig. 4.8 (neutral bent and charged linear) both the bending and the charge injection, lower the energy level of the LUMO. This means that both charge transfer and bending

activate CO_2 sinergically.

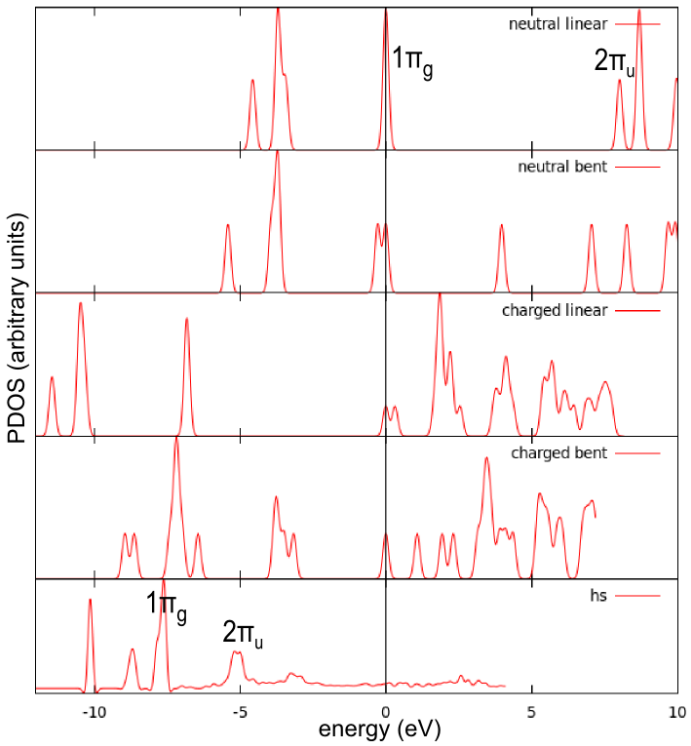

Figure 4.8: *Projected density of states of free CO_2 molecule, in neutral linear configuration, neutral bent configuration (with the fixed geometry of the charged bent configuration), charged linear configuration (with the fixed geometry of the neutral linear configuration), charged bent configuration and the chemisorbed CO_2 on Ni(110) HS configuration at 1/9 ML coverage. The origin is fixed to the Fermi energy of the system of molecule adsorbed on the surface.*

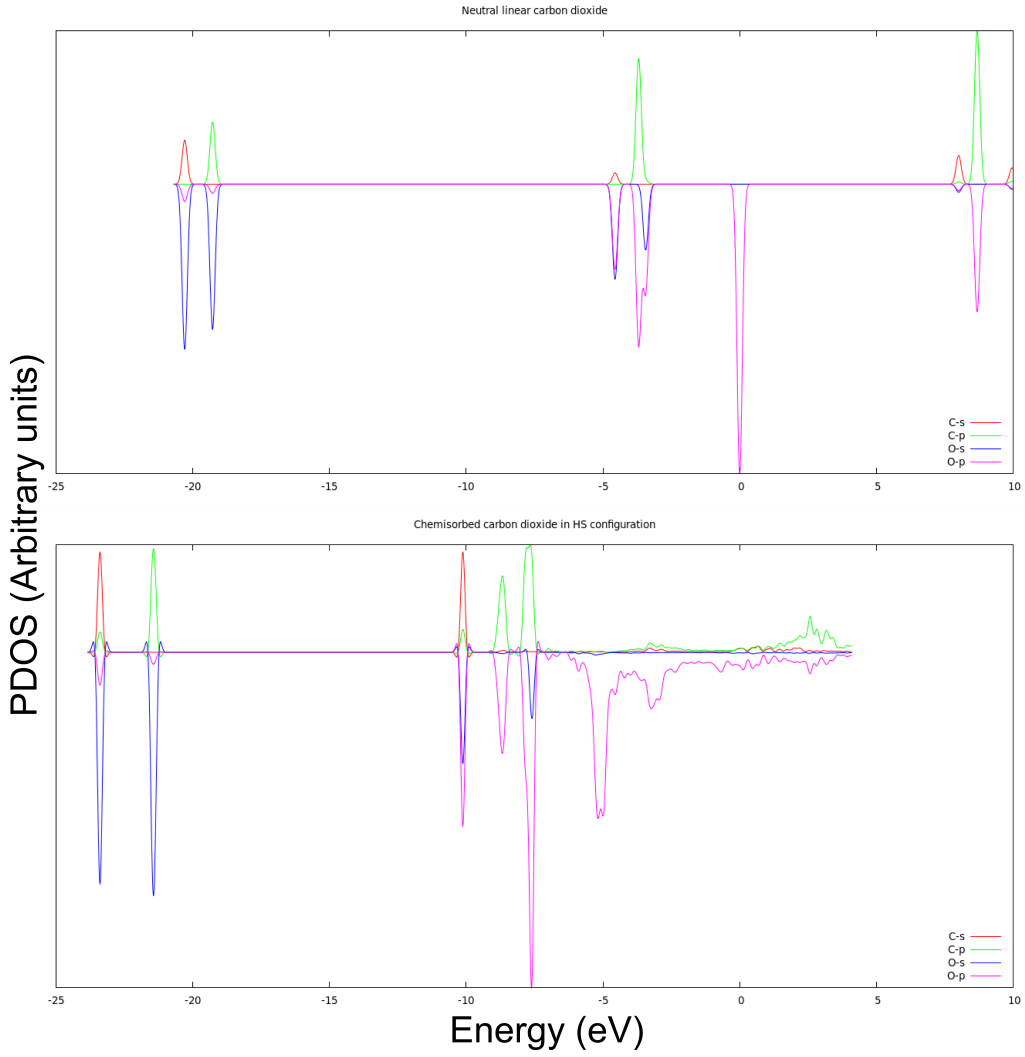

Figure 4.9: *Projected density of states of free CO_2 molecule in neutral linear configuration (upper panel), and the chemisorbed CO_2 on Ni(110) HS configuration at 1/9 ML coverage (lower panel), resolved onto atomic orbitals 2s and 2p. The origin is fixed to the Fermi energy of the system of molecule adsorbed on the surface, the carbon-PDOS are plotted upward and oxygen-PDOS are plotted downward.*

4.4 STM imaging

This section reports the simulation of STM images of the chemisorbed configurations and the comparison with the first low-temperature experimental images [36]. We first briefly report the experimental results, since our simulations of complex structures were suggested by the analysis of experimental images. The comparison allows the first and direct confirmation of the peculiar features of chemisorbed configurations of CO_2 on Ni(110).

4.4.1 Experimental LT-STM

An STM image of the surface after exposing the Ni sample to 0.17 L of CO_2 at T = 110K is shown in Fig.4.10 (upper left panel). Two different species adsorbed along the Ni troughs, a bright and a dim one, are clearly distinguishable. Close inspection of several experimental images indicates that the dim species are characterized by a dark halo, symmetric with respect to the underlying Ni atomic troughs, whereas the halo of the bright species is symmetric with respect to an axis rotated by about $\pm 45^\circ$ from the the [001] direction. While the dim molecules can be found as single, isolated units (Fig.4.10(c)), the bright molecules appear only within characteristic complexes of 2 (Fig.4.10(b)) or 3 (Fig.4.10(a)) molecules. The 2-molecule unit is formed by a bright and a dim species, and is arranged so that the dimer axis forms an angle of about $\pm 45^\circ$ with respect to the atomic rows. The 3-molecule unit is formed by two bright and one dim species, arranged in a V-shaped fashion with the vertex pointing along the [110] (as in Fig. 4.10(a)) or along the [001] direction. In the images, the bright species is characterized by a different position with respect to the substrate unit cell. This can be seen on the dashed-line inset in Fig. 4.10, where a calibrated grid,

with the crossing points of the vertical and horizontal lines corresponding to the positions of the surface Ni atoms, has been superimposed. Close inspection of the experimental STM images allowed us to infer that both species are adsorbed in hollow sites but with different geometry: the dim species is adsorbed symmetrically at the center of the unit cell, while the bright species appears slightly shifted off-center towards one of the Ni atoms at the corners of the unit cell.

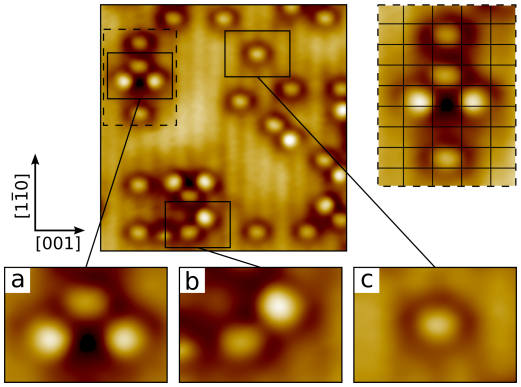

Figure 4.10: *STM image (top left,* $5.2 \times 5.2\,\mathrm{nm}^2$*) of* CO_2 *(*$0.05\,\mathrm{ML}$ *coverage) adsorbed on Ni(110) at* $110\,\mathrm{K}$*. Two non-equivalent* CO_2 *species can be distinguished from their apparent height. Close-ups (*$1.4 \times 1.0\,\mathrm{nm}^2$*) of the 3-molecule (a), the 2-molecule (b), and the single molecule units (c) are shown in the bottom row. In the dashed line inset (top right,* $1.6 \times 2.2\,\mathrm{nm}^2$*) the crossing points of the grid correspond to the positions of the substrate Ni atoms. (sample bias* $V = -10\,\mathrm{mV}$*,* $I_t = 1\,\mathrm{nA}$*).*

4.4.2 DFT simulations

We have simulated the STM images of all the four predicted chemisorption configurations for the isolated molecule and several 2- or 3-molecule complexes. The

two-molecule complexes was simulated in a 4×4 in-plane periodicity supercell, whereas the three molecule complexes in a 5×5 supercell. The images were simulated using the Tersoff-Hamman approximation [40]. A systematic comparison between the experimental images and the calculated adsorption geometries, with careful attention to the alignment of the symmetry axes with respect to the crystallographic directions of the Ni substrate, indicates that the dim species corresponds to the HS configuration and the bright species to the HU-s or HU configuration. On the basis of this attribution, a remarkable agreement is obtained when comparing the experimental and simulated images as shown in Fig.4.11. In the 3- or 2-molecule complexes (Fig. 4.11(a), (b)), one molecule clearly corresponds to HS. The other(s) could be either HU or HU-s, since the simulated STM images in the two cases appear almost identical (HU-s was used for the simulated images shown). The only difference is a very small mutual attractive interaction (about 0.05 eV) for the HS+HU-s pair with respect to the sum of the individually adsorbed molecules, at variance with HS+HU configuration. The triplet configuration is particularly stable, with an energy gain of about 0.2 eV with respect to the sum of the three molecules adsorbed apart, both considering HU or HU-s. The simulated images of pairs and triplets show very clearly a deep depression in between the adsorbed molecules of the complexes, closely resembling the experimental pattern. DFT simulations allow us to infer that the dark halo surrounding the isolated molecule, as well as the darker regions in the complexes, are originated by the electron transfer from the neighboring surface Ni atoms to the adsorbed molecules as already discussed in Sect. 4.3.1 (see Tab. 4.3).

With concern to the energetics of the adsorbed species, it is clear from the im-

ages that the experimentally most common configuration is the HS, at variance with what suggested by numerical simulations. The origin of this discrepancy can be discussed as follows. Firstly, it is important to recall that the variations of the calculated adsorption energy in the different configurations are comparable with the uncertainty due to physical approximations, as already pointed out, and therefore care has to be taken in considering the energy differences of the four configurations, for example in the LDA approximation HS is the most stable configuration. Secondly, kinetic effects (e.g. diffusion, dissipation) may steer the adsorption process towards adsorption phases which are not at the thermodynamic equilibrium. Finally, we note that the HU and HU-s chemisorbed states have a larger distance from the Ni surface than HS (see Tab. 4.1) and therefore are more exposed to the influence of the scanning STM tip, which may induce desorption, site switching or diffusion. Even though the existence of SB configuration is suggested by HREELS spectra (sec. 4.5), SB site appears to be extremely rarely occupied in STM images, even less than HU and HU-s. This has to be taken with caution: since the SB species shows the largest distance from the Ni surface, a tip induced site change may again explain the discrepancy. Moreover, SB configuration shows the largest ZPE (tab.4.4) that in turn could produce instability.

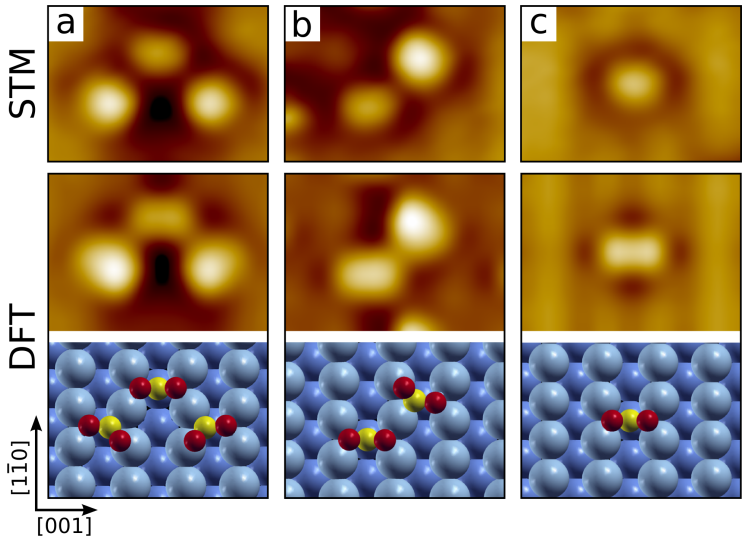

Figure 4.11: *Close-ups from Fig. 4.10 showing the experimental (top row) and DFT calculated (middle row) STM images of the 3-molecule (a), the 2-molecule (b) and the single molecule units (c). The bottom row shows ball models of the calculated geometries of the three units.*

4.5 Vibrational properties and zero point energy

Vibrational modes and frequencies were calculated within the DFT-Perturbation Theory [41], without DFT-D correction. The dynamical matrix was constructed from the forces due to independent off-equilibrium displacements of C, O, and the first layer Ni atoms. As a benchmark, the three normal vibration modes of linear, neutral, and free CO_2 were calculated within GGA and found equal to 80, 160, and 288 meV for the bending, the symmetric stretching, and the asymmetric stretching modes. The numerical accuracy associated to the calculated frequencies is $\pm$ 2 meV. The normal mode frequencies for the isolated molecule are in good agreement with the experimental values for the gas phase of 83, 165, and 291 meV, respectively [42]. The calculated vibrational frequencies for the chemisorbed and physisorbed configurations are shown in Tab. 4.4 and compared with the experimental data (fig. 4.12) already reported in Ref. [3]

HU and SB chemisorbed configurations are characterized by very similar frequencies of the normal modes; differences between HU and SB clearly beyond the numerical uncertainty are found for the asymmetric stretching mode (40 meV) and, to a less extent, for the bending mode (10 meV). As can be seen from Tab.4.4 the configuration with linear, neutral, and weakly bound CO_2 , far apart from the surface, is characterized, as expected, by the same frequencies calculated for the free molecule and the corresponding values can be unambiguously identified in the experimental HREELS spectra. We additionally point out that the measured 168 meV peak is also compatible within the experimental and numerical accuracy with the asymmetric stretching mode of HU-s and HS configurations

Table 4.4: *Calculated vibrational frequencies (in* meV*) of the various adsorption geometries in GGA approximation, compared with experiments.*

Mode	HU	HU-s	SB	HS	expt.	phys.	expt.
asymm. stretch	173	166	216	164	168	287	290
symm. stretch	136	123	140	134	141	160	168
bending	88	87	80	86	81-90	79	81
hind. rotation	50	46	63	50	-	78	-
ext. stretch	44	42	39	42	46	25	-
ZPE	245	232	269	238		314	

(besides HU), the 141 meV peak with the symmetric stretching mode of HS (besides HU and SB) and the 90 meV peak with the bending mode of HU-s and HS configurations (besides HU); the peak at 46 meV is compatible with the external stretching of all the four chemisorbed configurations.

The peak at 81 meV was correlated both to the linear, physisorbed configuration and to the SB configuration. It cannot be immediately attributed to any of the other chemisorbed configurations (HS, HU-s, and HU) since their calculated bending mode frequencies (86-88 meV) are rather higher with respect to the SB mode (80 meV). The presence of the 81 meV peak also at very low coverage (i.e. < 0.1 ML), where the physisorbed species is known to be absent, was interpreted as the fact that the SB species was already present in these conditions on the Ni surface.

The calculated vibrational frequencies can be used to estimate the zero point energy (ZPE) (last line of tab. 4.4), that is, the total vibrational energy at

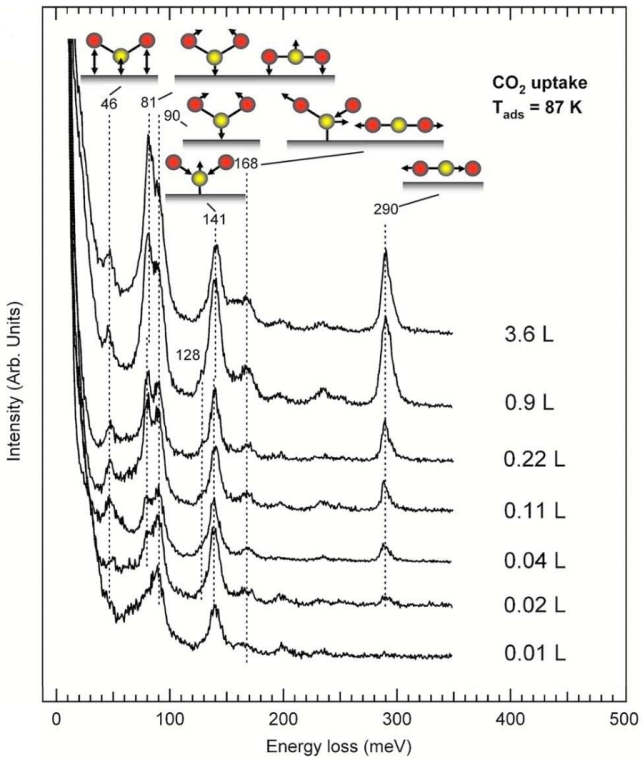

Figure 4.12: *HREELS spectra on Ni(110) as a function of the initial CO_2 exposure at 87 K [3].*

absolute zero (0 K). For each configuration ZPE was calculated as

$$E_{ZPE} = \frac{1}{2} h \sum_i \nu_i$$

where ν_i are the different vibrational frequencies.

We can further improve the estimate of adsorption energies correcting with the proper ZPE all the energies involved in eq. 4.1: neglecting the slow vibrations of the slab, the net result is an additional energy shift towards lower energies for the relative energies of chemisorbed configurations, since the ZPE correction for the isolated, linear, gas phase molecule is larger than for the adsorbed configurations (tab. 4.4). With this correction the average chemisorption energy amounts to 0.65

States	$E_{\text{ads}}^{\text{DFT-D}}$(eV)	$E_{\text{ads}}^{\text{DFT-D+ZPE}}$(eV)
HU	0.66	0.73
HU-s	0.60	0.69
SB	0.52	0.58
HS	0.50	0.58
phys.	0.29	0.29

Table 4.5: *DFT energies for the adsorption states of CO_2 on Ni(110) with a coverage of $\frac{1}{6}$ ML. DFT-D results without (first column) and with (second column) ZPE correction.*

eV, still comparable with the experimental estimate (0.60 eV) of the desorption energy.

4.6 Energy barriers

Several NEB calculations were performed to understand the activation-adsorption mechanism. The barrier between the physisorbed state (not activated, see Fig. 4.2) and the four chemisorbed configurations was calculated within both standard GGA and DFT-D corrected GGA, and we found almost identical results for the van der Waals corrected and uncorrected calculations. All the four chemisorption configurations have the same transition state (Fig. 4.13), that we first identified studying with NEB the physisorbed → SB process, corresponding to a barrier of 0.12 eV in DFT-D and 0.15 eV in GGA. [3]

[3]We performed NEB calculation between physisorbed → HS, physisorbed → HU-S and physisorbed → HU finding respectively the barriers of 0.40 eV, 0.21 eV, 0.35 eV. Then we checked that between the TS of process physisorbed → SB and the other chemisorbed configuration is

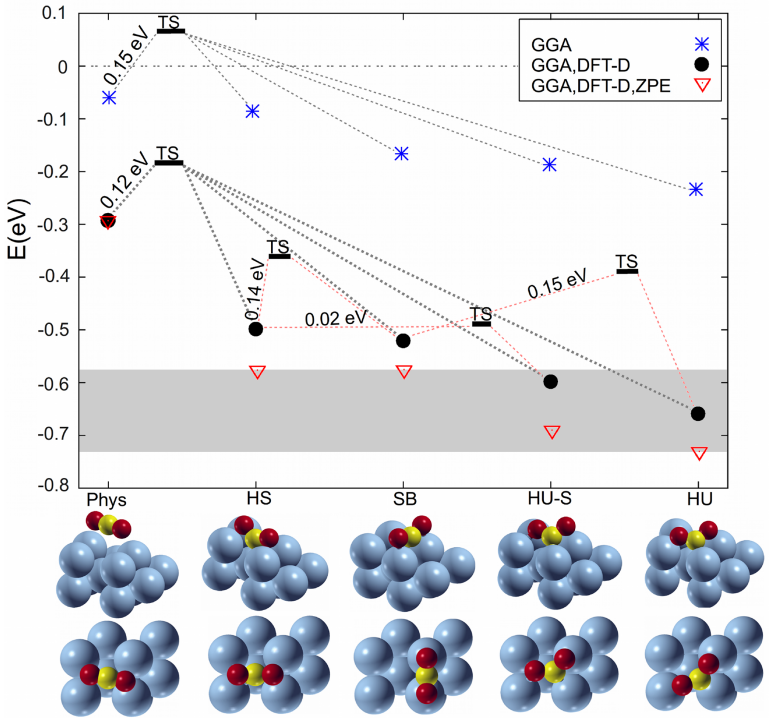

Figure 4.13: *Energy diagram for different CO_2 adsorption configurations on Ni(110) and relevant adsorption and diffusion barriers, calculated using DFT both with standard GGA and with DFT-D-corrected GGA. DFT-D energies including the ZPE contributions are also reported. The shaded region highlights the energy range of all the chemisorbed configurations in the latter approximation. The zero of the energy is set to the non-dissociated molecule at infinite distance from the surface.*

Figure 4.14 shows the adsorption process in SB configuration: TS is characterized by a distance carbon atom-surface of 2.13 Å and a bending angle of 166°. The transition state is characterized by sudden changes of the O-C-O bond angle and charges (see Fig.4.15) with respect to the gas phase, indicating that

almost zero

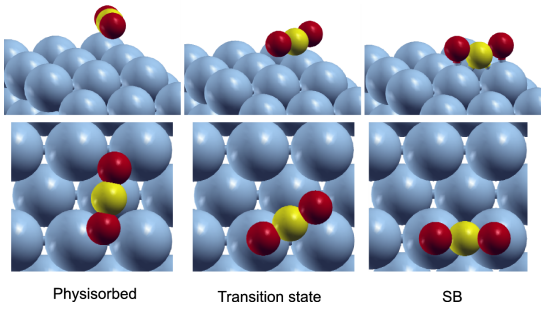

Figure 4.14: *Perspective and top view of ball models of initial state, TS and final state for the process: physorbed* $CO_2 \rightarrow$ *chemisorbed* CO_2 *in SB .*

bending and electron transfer are two important features in the chemisorption process, as already seen in 4.3.2 from static calculations. At variance with standard GGA calculations [3], DFT-D predicts that the chemisorption processes are non-activated, the difference being due not to the differences between the adsorption barriers calculated in the two approximation, but rather to the stronger adsorption DFT-D energies. This means that the desorption energies for DFT-D are equal to the adsorption energies, and in agreement with the experimental ones. (See 4.2)

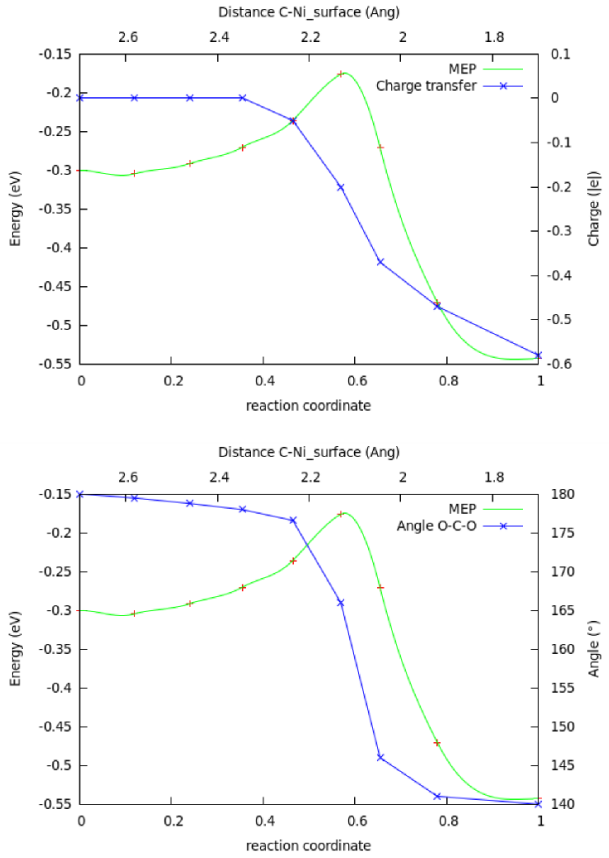

Figure 4.15: *Energy, charge transfer (upper panel) and bending angle (lower panel) for the process: physisorbed* $CO_2 \rightarrow$ *chemisorbed* CO_2 *in SB along the minimum energy path calculated using NEB.*

Chapter 5

Hydrogen assisted transformations of CO_2 on Ni(110)

In this chapter we study the hydrogenation of activated CO_2 species adsorbed on Ni(110) . We will compare the simulations with results coming from experiments performed using both molecular and atomic hydrogen. Molecular hydrogen doesn't react directly with adsorbed CO_2 but it firstly undergoes dissociative adsorption . The adsorbed hydrogen atoms (adsorption energy of $\approx$ 2.6 eV) then react with CO_2 on the surface (Langmuir-Hinshelwood mechanism (LH)). Atomic hydrogen, conversely, can directly react with adsorbed species before reaching the surface (Eley-Rideal mechanism (E-R)) (Fig. 5.1). This parallel study help us to understand the hydrogenation mechanisms at atomic level, and , in particular, to answer following questions that have attracted general attention:

1. *Does formate (COOH) react with H on nickel?*

2. *Is CO a reactive intermediate?*

3. *Does CO stem from formate decomposition?*

The main results presented in this chapter were published in The Journal of Physical Chemistry Letters [43].

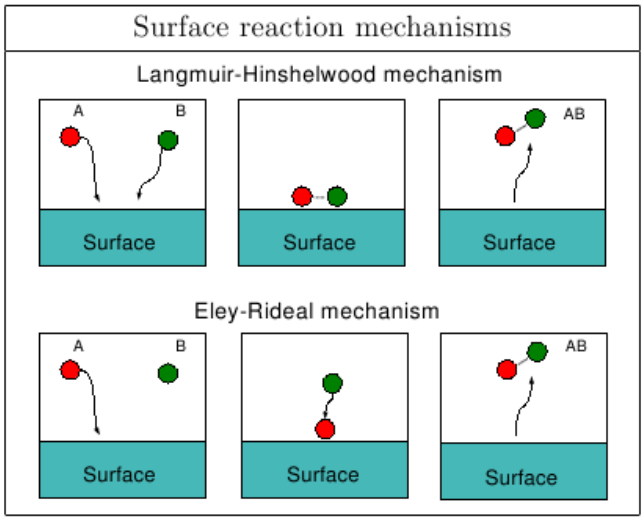

Figure 5.1: *Schematic representation of surface reaction mechanisms: Langmuir-Hinshelwood, where both molecules are adsorbed on the surface and then they undergo a chemical reaction, and Eley-Rideal, where only one molecule is adsorbed on the surface and the other one reacts directly with it, without adsorbing.*

5.1 Simulations

5.1.1 Technicalities

In this section different reactions between H and CO_2 are studied, in term of reaction barriers and characterization of the most relevant products and intermediates.

The calculations of reaction barriers were performed using the NEB method [22] (described in Sec.2.2), using 7 or 9 images, depending on the path reaction lenght, in a 3×2 supercell and relaxing the images in the paths until the forces orthogonal to the path were below 0.05 eV/Å. We use standard σ-GGA, without DFT-D correction, since it does not change significantly the barriers involved in the reactions.

5.1.2 Langmuir-Hinshelwood reactions

We first discuss LH reaction, starting from CO_2 and H coadsorbed (Fig. 5.1). Isolated H atom adsorbs preferentially in a hollow pseudo-3-fold site (in agreement with literature data [44]) followed by the long bridge and the short bridge sites, characterized respectively by adsorption energies of 2.68, 2.64, and 2.62 eV referred to an H atom in the gas phase far apart from the surface. After dissociative adsorption H atoms diffuse on surface overcoming barriers of ≈0.1 eV between the almost energetically equivalent three local minima and eventually react with a CO_2 molecule interacting with the C atom or one of the O atoms. Following a chemical/physical intuition we argue that possible products of this reaction are the formate (HCOO) and the hydrocarboxyl (HOCO), generated respectively through the interaction with C and O.

In order to study the details of the two channels of the CO_2 hydrogenation process, we consider the CO_2 molecule in the most stable HU configuration and H in the SB sites as indicated in Fig. 5.2, corresponding to the energetically most favored initial coadsorption configurations: one NEB calculation (CO_2 + H $\longrightarrow$ HCOO) starts with H in position 1 that reacts with carbon, while another NEB calculation (CO_2 + H $\longrightarrow$ HOCO) starts with H in position 2 that reacts

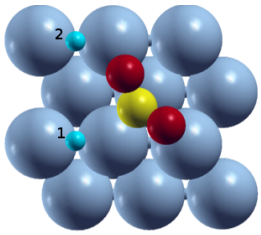

Figure 5.2: *Initial configurations for LH CO_2 hydrogenation: H in site 1 reacts with C or H in site 2 reacts with the upper O. Site 1 and 2 are SB sites.*

with the upper oxygen atom. In these geometries, the calculated adsorption energy of the coadsorbed CO_2 and H are, within our numerical accuracy, equal to the sum of CO_2 and H adsorbed separately. The structural adsorption details of the adsorbates are also unchanged, thus indicating that they do not interact.

The $CO_2 + H \longrightarrow HCOO$ transition state (Fig. 5.3, blue path on the left) involves a flip of H- CO_2 complex with a barrier of 0.43 eV. In principle, further reactions with adsorbed H atoms are possible: we calculated a barrier of 1.04 eV for the production of dioxomethylene (CO_2H_2) and of 0.80 eV for the production of formic acid (HCOOH) (Fig. 5.3, blue paths from the center to the right). However, these processes are in competition with the C-H cleavage in HCOO/Ni(110) ($\approx$1 eV). Moreover, the dissociation reactions $HCOOH \longrightarrow HCO + OH$ has a barrier of 0.40 eV (not shown in Figure), suggesting that the formic acid possibly formed in this process is unstable and prefers to dehydrogenate back to formate. Finally, we found that the dissociation of formate into CO is highly forbidden (barrier > 3 eV). We conclude that formate is a rather stable product of the CO_2 hydrogenation with coadsorbed H reacting with C.

An alternative CO_2 hydrogenation path involves a different LH process (Fig. 5.3, grey path). H reacts with an oxygen atom of the CO_2 molecule, overcoming

reactants, intermediates and products energy	(eV)
$CO_2 + 2\,H(g) + H$	-2.60
$CO_2 + H(g) + 2\,H$	-5.20
$HOCO^* + H(g) + H$	-4.82
$HOCO + H(g) + H$	-5.13
$HCOOH + H(g)$	-5.03
$H_2CO_2 + H(g)$	-5.39
$HCOO + H(g) + H$	-5.73
$CO + OH + H(g) + H$	-5.85
$CO + H_2O + H$	-5.90

Table 5.1: *Calculated DFT-GGA energies of the relevant reactants, intermediates, and products participating in the CO_2 hydrogenation on Ni(110) (same energy zero as in Fig. 5.3)*

a barrier of 0.52 eV in close competition with CO_2 dissociation and desorption (see Sec. 4.6). This yields the formation of a reactive hydrocarboxyl (HOCO) intermediate, which can be subsequently hydrogenated with a barrier of 0.48 eV to formic acid, that finally can easily decompose with production of formate.

In conclusion, our results indicate that at low temperature, formate is very stable against further LH reaction with hydrogen and does not yield CO directly upon decomposition. In Table 4.2, we report the energies of the configurations shown in Fig. 5.3.

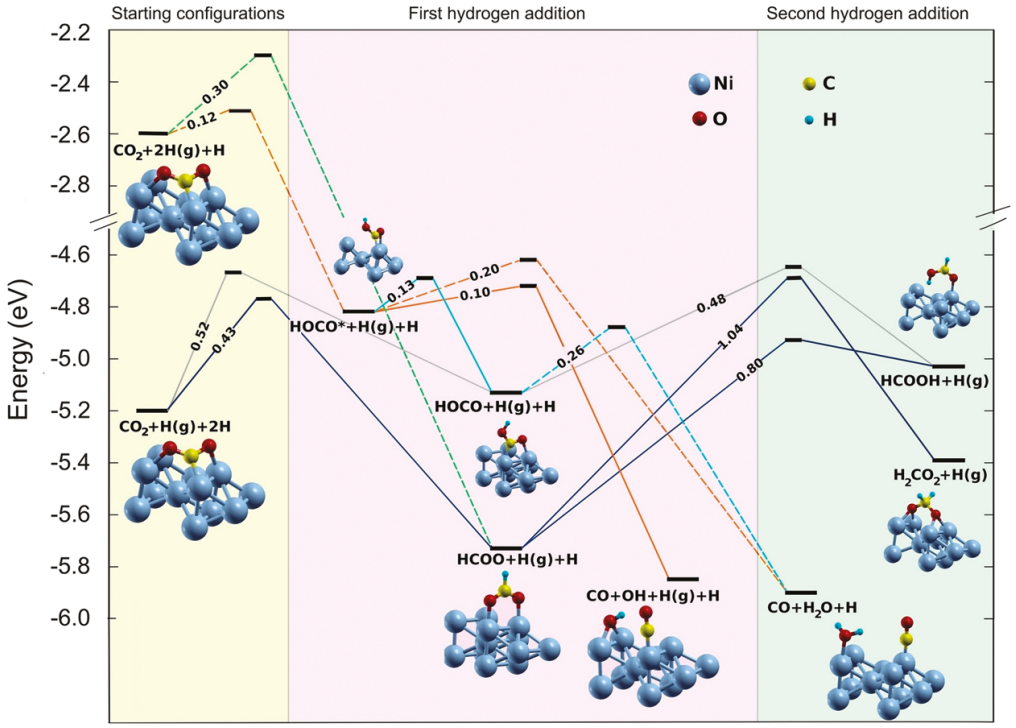

Figure 5.3: *Energy diagram obtained by DFT-GGA calculations. Different possible CO_2 hydrogenation pathways on Ni(110) are indicated with solid and dashed lines for LH and ER mechanisms, respectively. Colors indicate different reaction pathways according to the text. Energies are given with respect to gas-phase (g) atomic H and chemisorbed CO_2.*

5.1.3 Eley-Rideal reactions

In order to study reactions between gas phase hydrogen and adsorbed CO_2 (Eley-Rideal (ER) reactions, Fig. 5.1) we performed NEB calculations with H atom initially in the vacuum, at ≈ 6Å from the surface. Since there is no local minima in the vacuum to be considered as reference from which to start reactions, we carried out different preliminary NEB calculation for each reaction with different

starting H positions in x-y plane, then refining those with a lower barrier.

Experimentally these reactions may be favored by those H atoms which do not react immediately with CO_2 and are trapped by the Ni surface underneath. After dissipating part of their energy, they react in a 'hot' state with coadsorbed molecules [45, 43]. For this reason the calculated ER barriers (Fig. 5.3) are referred to the minimum that the ER-MEPs (Fig.5.4) exibit after an attractive potential well of almost 1 eV.

The path originated from the interaction H-O starts with a very small barrier (0.12 eV): we found an ER reaction channel yielding very stable coadsorbed CO and OH or water via a hydrocarboxyl precursor (HOCO*) (Fig. 5.3, orange path). Alternatively, HOCO* can evolve into a more stable HOCO configuration, leading to CO and H_2O after a second hydrogenation (cyan path). Similar paths are suggested with the support of DFT and microkinetic modeling for the reverse water gas shift reaction on Pt catalysts [46].

The interaction H-C, with a 0.30 eV barrier for the first CO_2 ER hydrogenation, directly produces formate (green path in Fig. 5.3). The energy barriers given above are small with respect to the kinetic energy that the impinging H atoms gain due to the attractive potential well of the metal surface (as we can see in fig.5.4 that shows the MEP of reaction). In particular, the first ER reaction step is thus easily accessible already at liquid nitrogen temperature.

5.2 Experimental results

Two kind of experiments was performed to study the CO_2 hydrogenation on Ni(110), using molecular and atomic hydrogen and collecting TPD, XPS and HREELS spectra.

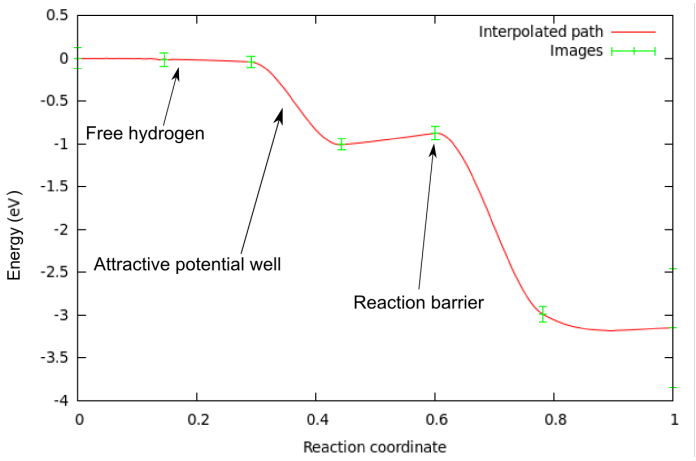

Figure 5.4: *Minimum Energy Path (MEP) profile for the reaction* $CO_2 + H(g) \longrightarrow HOCO^*$

With respect to the TPD spectra in Fig. 4.5, after dosing molecular or atomic hydrogen a new feature appears in the CO_2 TPD spectra at 305 K at the expense of the 220 K state, suggesting the formation of a reaction intermediate [15, 43] that dehydrogenates at 305 K.

From XPS spectra, we can state that this intermediate is the formate (HCOO), produced after annealing up to 155 K using molecular hydrogen (LH reactions, Fig. 5.5), but is already present at 90 K using atomic hydrogen (ER reactions, Fig. 5.6). This is consistent with the difference between the calculated energy barriers for the formate production, 0.43 eV and 0.30 eV (Fig. 5.3). The HREELS spectra confirm the presence of formate already at 90 K for atomic hydrogen (365 meV peak, C-H stretching). In Fig. 5.7 we clearly distinguish the carbon monoxide C-O stretching peak and the water and OH O-H stretching peak, present at 90 K only in the case of hydrogenation with atomic hydrogen (right panel), in agreement with results of our simulations (Fig. 5.3).

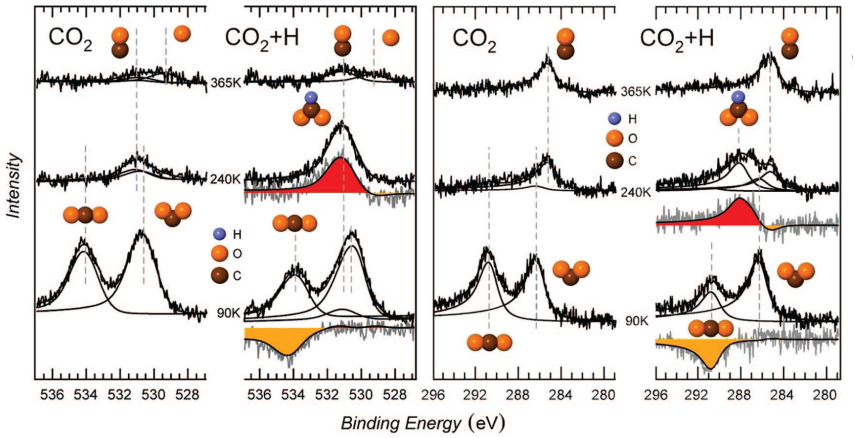

Figure 5.5: *Spectroscopy data collected upon stepwise annealing of the CO_2 covered Ni(110) surface and of the CO_2+H coadsorbed layer after molecular hydrogen deposition: XPS spectra of the O (left) and C (right) 1s core levels; the gray curves are difference plots between same-temperature XPS spectra of the CO_2 + H layer and of the pure CO_2 layer; additional (red) and missing (yellow) contributions are highlighted* [15].

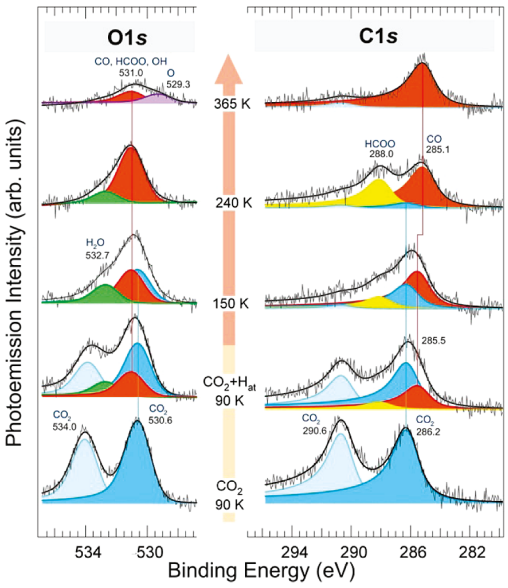

Figure 5.6: *XPS spectra. O1s (left panel) and C1s (right panel) corelevel spectra of the CO_2/Ni(110) and $CO_2 + H_{at}$/Ni(110) layers as a function of the annealing temperature; best fit curves and contributions as obtained by the fitting procedure are shown* [43].

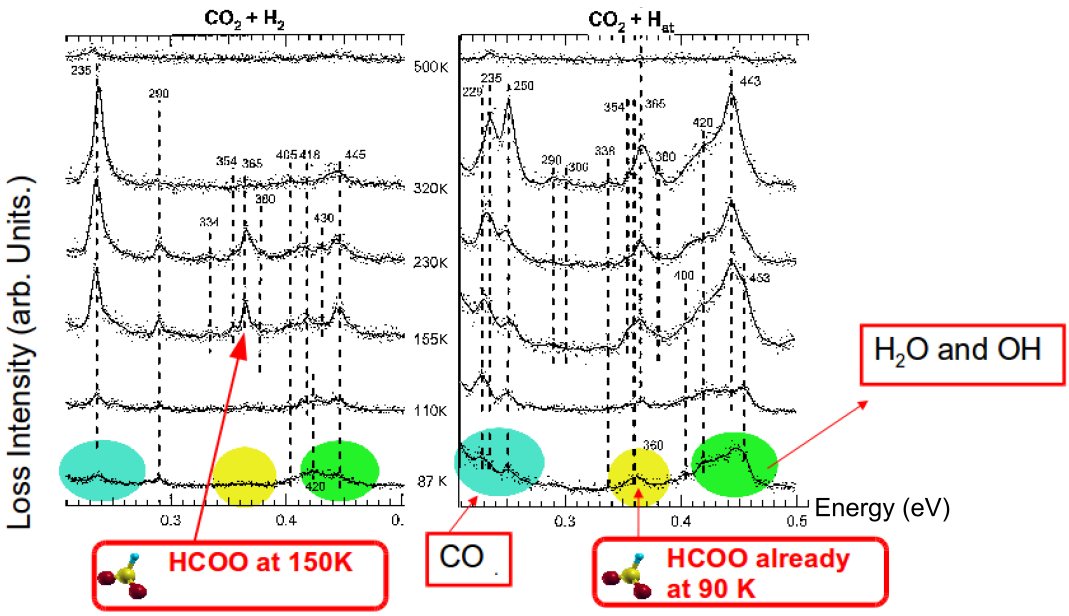

Figure 5.7: *HREELS spectra of the $CO_2 + H_2$/Ni(110) layers (left) and $CO_2 + H_{atomic}$/Ni(110) layers (right) as a function of the annealing temperature* [15, 43].

Chapter 6

Conclusion

Using ab-initio DFT calculations, both within the standard GGA for the exchange-correlation functional and with the DFT-D correction for the Van der Waals contribution we have studied CO_2 adsorption and hydrogenation on Ni(110) ideal surfaces. Calculations predict four almost energetically equivalent chemisorbed configurations for CO_2 adsorption on Ni(110). Three of the predicted adsorption geometries are consistent with the experimental STM images, namely HU, HU-s and HS species. The DFT-D adsorption energy values, corrected also with the ZPE, are in good agreement with the TPD data. Accounting for the new adsorption configurations found in this thesis, we could refine the assignment of the vibrational modes observed in previous HREEL spectra. The sinergic roles of charge and bending of the adsorbed CO_2 are discussed in detail by studying electronic structure.

We have analyzed at the atomic scale the mechanisms of the $CO_2 + H$ reaction network on Ni(110) under UHV conditions. In particular, we have demonstrated that (i) CO is an intermediate in the most favorable ER reaction paths, (ii) the adsorbed CO intermediate stems from ER hydrogenation of CO_2 at low temper-

ature and not from formate, and (iii) in all reaction schemes, formate is present and acts as a very stable spectator, with high and comparable LH reaction barriers for both dehydrogenation and further hydrogenation. In this study we have provided direct evidence for a hydrogen-assisted CO_2 activation mechanism yielding C-O bond cleavage via a carboxyl intermediate. The results provide insight into the CO_2 catalytic conversion reaction, offering (i) consistent and solid support to the previously proposed hypothesis that formate is not an intermediate of the CO_2 hydrogenation process and (ii) a detailed reaction mechanism which is compatible with all of the observations obtained under experimental working conditions.

We are aware that the study of catalytic reactions is affected by the well known 'material gap' and 'pressure gap' problems, i.e. the difficulty of transferring results obtained on model catalysts (single crystal, perfect surfaces, ultra high vacuum (UHV) condition) to catalysis in real environment.

The study of the interaction of CO_2 with more complex Ni-based structures, closer to real systems, such as mixed Ni-Cu substrates and Ni nano-clusters on insulating supports, however, goes in the direction of accounting for the 'material gap'.

To this purpose some work is in progress to study the CO_2 adsorption on Ni/Cu(110) surface. As already said in the introduction, a Ni-Cu alloy has been shown to be an active catalyst for methanol synthesis [11, 12, 13]. Bimetallic surfaces play a decisive role in heterogeneous catalysis. Due to the particular arrangement of the different atoms at the surface, new reaction pathways can be opened and both the activity and selectivity of catalysts can be improved. Various concepts for the specific reaction properties of bimetallic surfaces have

been discussed in the literature [47, 48, 49, 50, 51]. The Ni/Cu system is a very attractive model system of bimetallic surfaces: these bulk metals have the same structure and similar lattice parameter; on the other hand their electronic and magnetic properties are very different. This is what makes the bimetallic surfaces so attractive because one can expect to be able to tune the surface reactivity at will, in searching different catalytic properties.

The reactivity property of bimetallic surfaces, however, are not simply linear interpolation of the properties of their constituents. Preliminary results for adsorbed CO and CO_2 indicate a stronger molecule-metal bond at selected Ni/Cu alloy surface configurations, not only with respect to the pure Cu termination where it is known that chemisorption does not occur, but also with respect to pure Ni termination. For example, from our preliminary tests, it results that CO_2 adsorbs stronger on 1ML of Ni deposited on Cu(110) than on clean Ni(110).

These results indicate the importance electronic structure detail in order to enhance the catalytic activity and confirm the trend already observed in other bimetallic alloys. i.e., that the deposition of a more reactive metal (e.g., Ni) onto a less reactive metal substrate (e.g., Cu) makes the overlayer even more reactive with respect to adsorption and suggest the origin of the observed peculiar reactivity of Ni/Cu alloy.

The real catalysts are not single crystals, for example powders are used. In order to face this aspect of the 'material gap', with respect to our problem, the adsorption of CO_2 on a more realistic model supported catalyst can be studied, for example Ni clusters on a thin MgO film deposited on Ag(100). Oxide-based films are indeed excellent matrix for nanoparticles and clusters deposition, allowing controlled growth of a supported model-system catalyst under UHV

[52, 53]. At present, while Ni clusters have been studied by STM on alumina and on TiO_2 [54], work with MgO substrate don't exist, although high pressure tests demonstrate that supported on MgO nanoparticles have high reactivity with respect to CO dissociation [55] and methane reforming [56]. In particular aspects not yet explored concerning the Ni nano-clusters on MgO/Ag(100) films in UHV are:

-Cluster nucleation on substrate-structure.

-Structure, dimension and distribution of the Ni clusters.

-Mechanism involved in the reaction $CO_2 + H_2$.

The long-standing question about the transferability of the results obtained under ultra high vacuum conditions to real systems would suggest to extend the simulation of carbon dioxide reduction at Ni or Cu/Ni surfaces in a liquid environment under electrocatalytic conditions. Several efforts have been made recently in order to afford electronic-structure calculations in solution. A 'natural' but 'brute-force' answer to this problem is to explicitly include the solvent molecules in the system, either as one or several solvation shells or as a bulk medium that fills the simulation box in periodic-boundary conditions . This approach has been successfully followed in some cases (e.g. [57] but it becomes prohibitively expensive if one wants to use it systematically for a good statistics. Alternative to this explicit approach, recent efforts have been made [58] starting from a description of the solvent as a continuum dielectric medium surrounding a quantum-mechanical solute [59], then combined with a first-principles formulation of the cavitation energy based on a quantum-mechanical definition for the surface of a solute and implemented in the Car-Parrinello framework in QE [60, 61] and recently revised and improved for efficient applications to solid-liquid interfaces [62]. The use of

hybrid quantum-mechanical/ molecular-mechanics (QM/MM) techniques [63] is also an alternative approach towards realistic electrochemistry.

Bibliography

[1] H. J. Freund and M. W. Roberts, "Surface chemistry of carbon dioxide," *Surface Science Reports*, vol. 25, no. 8, pp. 225–273, 1996.

[2] B. Bartos, H.-J. Freund, H. Kuhlenbeck, M. Neumann, H. Lindner, and K. Muller, "Adsorption and reaction of CO_2 and CO_2/O CO-adsorption on Ni(110): Angle resolved photoemission (ARUPS) and electron energy loss (HREELS) studies," *Surface Science*, vol. 179, no. 1, pp. 59–89, 1987.

[3] X. Ding, L. D. Rogatis, E. Vesselli, A. Baraldi, G. Comelli, R. Rosei, L. Savio, L. Vattuone, M. Rocca, P. Fornasiero, F. Ancilotto, A. Baldereschi, and M. Peressi, "Interaction of carbon dioxide with Ni(110): A combined experimental and theoretical study," *Phys. Rev. B*, vol. 76, no. 19, p. 195425, 2007.

[4] X. Ding, V. Pagan, M. Peressi, and F. Ancilotto, "Modeling adsorption of CO_2 on Ni(110) surface," *Mater. Sci. Eng. C*, vol. 27, pp. 1355–1359, September 2007.

[5] G. Illing, D. Heskett, E. Plummer, H.-J. Freund, J. Somers, T. Lindner, A. Bradshaw, U. Buskotte, M. Neumann, U. Starke, K. Heinz, P. D. Andres, D. Saldin, and J. Pendry, "Adsorption and reaction of CO_2 on Ni(110): X-

ray photoemission, near-edge X-ray absorption fine-structure and diffuse leed studies," *Surface Science*, vol. 206, no. 1-2, pp. 1–19, 1988.

[6] S.-G. Wang, D.-B. Cao, Y.-W. Li, J. Wang, and H. Jiao, "Chemisorption of CO_2 on Nickel Surfaces," *The Journal of Physical Chemistry B*, vol. 109, no. 40, pp. 18956–18963, 2005.

[7] J. Hansen, *Handbook of Heterogeneous Catalysis*, vol. 4, pag. 1856. G. Ertl, H. Knötzinger and J. Weitkamp editors, 1997.

[8] P. Rasmussen, M. Kazuta, and I. Chorkendorff, "Synthesis of methanol from a mixture of H_2 and CO_2 on Cu(100)," *Surface Science*, vol. 318, no. 3, pp. 267–280, 1994.

[9] A. A. Gokhale, J. A. Dumesic, and M. Mavrikakis, "On the mechanism of low-temperature water gas shift reaction on copper," *Journal of the American Chemical Society*, vol. 130, no. 4, pp. 1402–1414, 2008.

[10] A. Lapidus, N. Gaidai, N. Nekrasov, L. Tishkova, Y. Agafonov, and T. Myshenkova, "The mechanism of carbon dioxide hydrogenation on copper and nickel catalysts," *Petroleum Chemistry*, vol. 47, pp. 75–82. 10.1134/S0965544107020028.

[11] J. Nerlov and I. Chorkendorff, "Promotion through gas phase induced surface segregation: Methanol synthesis from CO, CO_2 and H_2 over Ni/Cu(100)," *Catal. Lett.*, vol. 54, no. 4, pp. 171–176, 1998.

[12] J. Nerlov and I. Chorkendorff, "Methanol Synthesis from CO_2, CO, and H_2 over Cu(100) and Ni/Cu(100)," *J. Catal.*, vol. 181, no. 2, pp. 271–279, 1999.

[13] J. Nerlov, S. Sckerl, J. Wambach, and I. Chorkendorff, "Methanol synthesis from CO_2, CO and H_2 over Cu(100) and Cu(100) modified by Ni and Co," *Appl. Catal. A*, vol. 191, no. 1 - 2, pp. 97–109, 2000.

[14] F. L. Peltier, P. Chaumette, J. Saussey, M. M. Bettahar, and J. C. Lavalley, "In situ FT-IR and kinetic study of methanol synthesis from CO_2/H_2 over $ZnAl_2O_4$ and Cu-$ZnAl_2O_4$ catalysts," *Journal of Molecular Catalysis A: Chemical*, vol. 132, no. 1, pp. 91–100, 1998.

[15] E. Vesselli, L. D. Rogatis, X. Ding, A. Baraldi, L. Savio, L. Vattuone, M. Rocca, P. Fornasiero, M. Peressi, A. Baldereschi, R. Rosei, and G. Comelli, "Carbon dioxide hydrogenation on Ni(110).," *J. Am. Chem. Soc.*, vol. 130, no. 34, pp. 11417–11422, 2008.

[16] P. Giannozzi, S. Baroni, N. Bonini, M. Calandra, R. Car, C. Cavazzoni, D. Ceresoli, G. L. Chiarotti, M. Cococcioni, I. Dabo, A. D. Corso, S. de Gironcoli, S. Fabris, G. Fratesi, R. Gebauer, U. Gerstmann, C. Gougoussis, A. Kokalj, M. Lazzeri, L. Martin-Samos, N. Marzari, F. Mauri, R. Mazzarello, S. Paolini, A. Pasquarello, L. Paulatto, C. Sbraccia, S. Scandolo, G. Sclauzero, A. P. Seitsonen, A. Smogunov, P. Umari, and R. M. Wentzcovitch, "QUANTUM ESPRESSO: A modular and open-source software project for quantum simulations of materials," *J. Phys.: Condens. Matter*, vol. 21, no. 39, p. 395502, 2009.

[17] P. Hohenberg and W. Kohn, "Inhomogeneous electron gas," *Phys. Rev.*, vol. 136, pp. B864–B871, Nov 1964.

[18] W. Kohn and L. J. Sham, "Self-consistent equations including exchange and correlation effects," *Phys. Rev.*, vol. 140, pp. A1133–A1138, Nov 1965.

[19] M. C. Payne, M. P. Teter, D. C. Allan, T. A. Arias, and J. D. Joannopoulos, "Iterative minimization techniques for ab initio total-energy calculations: molecular dynamics and conjugate gradients," *Rev. Mod. Phys.*, vol. 64, pp. 1045–1097, Oct 1992.

[20] K. J. Laidler and M. C. King, "Development of transition-state theory," *The Journal of Physical Chemistry*, vol. 87, no. 15, pp. 2657–2664, 1983.

[21] G. Henkelman, B. P. Uberuaga, and H. Jónsson, "A climbing image nudged elastic band method for finding saddle points and minimum energy paths," *The Journal of Chemical Physics*, vol. 113, no. 22, pp. 9901–9904, 2000.

[22] H. Jónsson, G. Mills, and K. W. Jacobsen, *Nudged elastic band method for finding minimum energy paths of transitions*, ch. Classical and Quantum Dynamics in Condensed Phase Simulations, pp. 385–404. Singapore: World Scientific, 1998.

[23] D. Vanderbilt, "Soft self-consistent pseudopotentials in a generalized eigenvalue formalism," *Phys. Rev. B*, vol. 41, pp. 7892–7895, Apr 1990.

[24] A. Kokalj, "Xcrysden–a new program for displaying crystalline structures and electron densities," *Journal of Molecular Graphics and Modelling*, vol. 17, no. 3-4, pp. 176 – 179, 1999.

[25] G. Makov and M. C. Payne, "Periodic boundary conditions in ab initio calculations," *Phys. Rev. B*, vol. 51, pp. 4014–4022, Feb 1995.

[26] J. P. Perdew, K. Burke, and M. Ernzerhof, "Generalized Gradient Approximation Made Simple," *Phys. Rev. Lett.*, vol. 77, no. 18, pp. 3865–3868, 1996.

[27] A. Baldereschi, "Mean-value point in the brillouin zone," *Phys. Rev. B*, vol. 7, pp. 5212–5215, Jun 1973.

[28] P.-O. Lowdin, "On the non-orthogonality problem connected with the use of atomic wave functions in the theory of molecules and crystals," *The Journal of Chemical Physics*, vol. 18, no. 3, pp. 365–375, 1950.

[29] J. P. Perdew and A. Zunger, "Self-interaction correction to density-functional approximations for many-electron systems," *Phys. Rev. B*, vol. 23, pp. 5048–5079, May 1981.

[30] D. E. Fowler and J. V. Barth, "Structure and dynamics of the Cu(001) surface investigated by medium-energy ion scattering," *Phys. Rev. B*, vol. 52, pp. 2117–2124, Jul 1995.

[31] H. J. Monkhorst and J. D. Pack, "Special points for brillouin-zone integrations," *Phys. Rev. B*, vol. 13, pp. 5188–5192, Jun 1976.

[32] G. Chiarotti and Landolt-Börnstein, *Physics of Solid Surfaces*, vol. 24 of *New Series*. Springer-Verlag, part c ed., 1995.

[33] F. Favot, A. Dal Corso, and A. Baldereschi, "Ab initio study of CO adsorption on Ni(110): Effects on surface magnetism at low coverage," *Phys. Rev. B*, vol. 63, p. 115416, Mar 2001.

[34] S. Yalisove, W. Graham, E. Adams, M. Copel, and T. Gustafsson, "Multilayer relaxations of Ni(110): New medium energy ion scattering results," *Surface Science*, vol. 171, no. 2, pp. 400–414, 1986.

[35] L. E. Petersen, C. S. Sorensen, and D. L. Adams, "Oscillatory relaxation of the Ni(110) surface: a LEED study," *Journal of Physics C: Solid State Physics*, vol. 18, no. 8, 1985.

[36] C. Dri, A. Peronio, E. Vesselli, C. Africh, M. Rizzi, A. Baldereschi, M. Peressi, and G. Comelli, "Imaging and characterization of activated co_2 species on ni(110)," *Phys. Rev. B*, vol. 82, p. 165403, Oct 2010.

[37] S. Grimme, "Semiempirical GGA-type density functional constructed with a long-range dispersion correction," *Cond. Mat. Phys.*, vol. 27, pp. 1787–1799, 2006.

[38] P. A. Redhead *Vacuum*, vol. 12, no. 203.

[39] D. Sanchez-Portal, E. Artacho, and J. M. Soler, "Projection of plane-wave calculations into atomic orbitals," *Solid State Communications*, vol. 95, no. 10, pp. 685–690, 1995.

[40] J. Tersoff and D. R. Hamann, "Theory of the scanning tunneling microscope," *Phys. Rev. B*, vol. 31, pp. 805–813, Jan 1985.

[41] S. Baroni, S. de Gironcoli, A. Dal Corso, and P. Giannozzi, "Phonons and related crystal properties from density-functional perturbation theory," *Rev. Mod. Phys.*, vol. 73, pp. 515–562, Jul 2001.

[42] G. Herzberg, *Infrared and Raman Spectra*. Van Nostrand, New York, 1945.

[43] E. Vesselli, M. Rizzi, L. D. Rogatis, X. Ding, A. Baraldi, G. Comelli, L. Savio, L. Vattuone, M. Rocca, P. Fornasiero, A. Baldereschi, and M. Peressi, "Hydrogen-Assisted Transformation of CO_2 on Nickel: The Role of Formate

and Carbon Monoxide," *J. Phys. Chem. Lett.*, vol. 1, no. 1, pp. 402–406, 2010.

[44] G. Kresse and J. Hafner, "First-principles study of the adsorption of atomic H on Ni(111), Ni(100) and Ni(110)," *Surface Science*, vol. 459, no. 3, pp. 287–302, 2000.

[45] E. Hasselbrink, "Non-adiabaticity in surface chemical reactions," *Surface Science*, vol. 603, no. 10-12, pp. 1564–1570, 2009. Special Issue of Surface Science dedicated to Prof. Dr. Dr. h.c. mult. Gerhard Ertl, Nobel-Laureate in Chemistry 2007.

[46] L. C. Grabow, A. A. Gokhale, S. T. Evans, J. A. Dumesic, and M. Mavrikakis, "Mechanism of the water gas shift reaction on pt: First principles, experiments, and microkinetic modeling," *The Journal of Physical Chemistry C*, vol. 112, no. 12, pp. 4608–4617, 2008.

[47] C. T. Campbell *Annu. Rev. Phys. Chem*, vol. 41, p. 775, 1990.

[48] D. W. Goodman *Surf. Sci.*, no. 299-300, p. 837, 1994.

[49] J. A. Rodriguez *Surf. Sci. Rep*, no. 24, p. 223, 1996.

[50] J. G. Chen, C. A. Menning, and M. B. Zellner *Surf. Sci. Rep.*, no. 63, p. 201, 2008.

[51] E. Demirci, C. Carbogno, A. Groß, and A. Winkler, "Adsorption of CO on $Ni/Cu(110)$ bimetallic surfaces," *PRB*, no. 80, p. 085421, 2009.

[52] M. Schmid, G. Kresse, A. Buchsbaum, E. Napetschnig, S. Gritschneder, M. Reichling, and P. Varga, "Nanotemplate with Holes: Ultrathin Alumina on $Ni_3Al(111)$," *Phys. Rev. Lett.*, vol. 99, p. 196104, Nov 2007.

[53] A. Winkler, H. Borchert, and K. Al-Shamery, "Oxidation and thermal stability of nickel deposited on a thin alumina support," *Surface Science*, vol. 600, no. 15, pp. 3036–3044, 2006.

[54] K. Fujikawa, S. Suzuki, Y. Koike, W.-J. Chun, and K. Asakura, "Self-regulated Ni cluster formation on the $TiO_2(110)$ terrace studied using scanning tunneling microscopy," *Surface Science*, vol. 600, no. 10, pp. 117–121, 2006.

[55] U. Heiz, F. Vanolli, A. Sanchez, and W.-D. Schneider, "Size-dependent molecular dissociation on mass-selected, supported metal clusters," *Journal of the American Chemical Society*, vol. 120, no. 37, pp. 9668–9671, 1998.

[56] B.-Q. Xu, J.-M. Wei, Y.-T. Yu, J.-L. Li, and Q.-M. Zhu, "Carbon Dioxide Reforming of Methane Over Nanocomposite Ni/ZrO_2 Catalysts," *Topics in Catalysis*.

[57] A. C. et al. et al. *J. Am. Chem. Soc.*, no. 132, p. 4790, 2010.

[58] I. Dabo, B. N., Y. Li, and N. Marzari, *Ab Initio Electrochemical Properties of Electrode Surfaces, in Fuel Cell Science: Theory, Fundamentals, and Biocatalysis*. John Wiley & Sons, Inc., 2010.

[59] J.-L. Fattebert and F. Gygi *Int. J. Quantum Chem.*, no. 93, p. 139, 2003.

[60] D. Scherlis, J.-L. Fattebert, F. Gygi, M. Cococcioni, and N. Marzari *J. Chem. Phys.*, no. 124, p. 074103, 2006.

[61] I. Dabo, E. Cances, N. Marzari, and Y. Li *arXiv*, no. 0901.0096v3, 2010.

[62] V. M. Sánchez *J. Chem. Phys.*, no. 131, p. 904, 2009.

[63] G. M. Monard *Acc. Chem. Res.*, no. 32, p. 904, 1999.

Acknowledgments

M.R. acknowledges the Sincrotrone Trieste S.C.p.A. for financial support (fellowship) during his PhD. This research was funded by MIUR PRIN2008. We acknowledge the CINECA award under the ISCRA initiative, for the availability of high performance computing resources and support. Computational resources have been also partly obtained within the agreement between the University of Trieste and the Consorzio Interuniversitario CINECA (Italy) and partly within the Standard HPC Grant initiative of CASPUR (Italy).